1983

Optimal tensioning of nonlinear antenna structures

Steven James Hooper
Iowa State University

Hooper, Steven James

OPTIMAL TENSIONING OF NONLINEAR ANTENNA STRUCTURES

Iowa State University PH.D. 1983

Optimal tensioning of nonlinear antenna structures

by

Steven James Hooper

A Dissertation Submitted to the
Graduate Faculty in Partial Fulfillment of the
Requirements for the Degree of
DOCTOR OF PHILOSOPHY

Major: Aerospace Engineering

Approved:

Signature was redacted for privacy.

In Charge of Major Work

Signature was redacted for privacy.

For the Major Department

Signature was redacted for privacy.

For the Graduate College

Iowa State University
Ames, Iowa

1983

TABLE OF CONTENTS

LIST OF SYMBOLS

A	cross sectional area
E	Young's modulus
$\bar{G}_{x_j}$	cable force in the x direction at node j
G_{y_j}	cable force in the y direction at node j
h_i	i^{th} equality constraint
t_L	element length at time t
R_{x_i}	applies nodal force in the x direction at node i
R_{y_i}	applies nodal force in the y direction at node i
$\tilde{R}_{x_i}$	cable nodal force in the x direction at node i
$\tilde{R}_{y_i}$	cable nodal force in the y direction at node i
u_i	displacement in the x direction at node i
v_i	displacement in the y direction at node i
x_i	coordinate of node i
y_i	coordinate of node i
x_{s_i}	coordinate of surface node i
y_{s_i}	coordinate of surface node i
ΔT	temperature change
$[B]$	strain displacement matrix
$[B_{NL}]$	nonlinear strain displacement matrix
$[D]$	elasticity matrix
$[D_{NL}]$	matrix of Cauchy stresses
$^{t+\Delta t}\{F\}$	vector of point forces corresponding to element stresses at time $t+\Delta t$

$^{t+\Delta t}[K_E]$	elastic stiffness matrix at time $t+\Delta t$
$^{t+\Delta t}[K_{NL}]$	geometrically nonlinear stiffness matrix at time $t+\Delta t$
$^{t+\Delta t}\{R\}$	vector of applied forces at time $t+\Delta t$
$[T]$	transformation matrix
$\{z\}$	search direction vector
$^{t+\Delta t}\{\Delta u\}$	displacement search direction at time $t+\Delta t$
α	step size
$\bar{\alpha}$	coefficient of thermal expansion
ε	convergence tolerance
ξ ζ	natural element coordinates
$^{t}\tau$	axial stress in the element at time t referred to time 0
χ_i	decision variable
χ^*	minimum point
∇	gradient operator

1. INTRODUCTION AND HISTORICAL OVERVIEW

One of the significant features of the high technology society in which we live is the communication revolution. This revolution results in an instant global communication capability for nearly every person in the industrialized world. One example of this technology is our ability to instantly call or wire another person anywhere in the world. Another example is the nightly televised news broadcast in which the events of the moment are communicated live around the world.

The technology described above is largely made possible by communication satellites located in geostationary orbits over the Earth. This technology will be exploited to an even greater extent in the near future with the development of electronic mail and computerized marketing systems.

Thompson and Schultz (1) point out the potential shortage of orbital parking spaces when using the current satellite technology level. The current system employs large ground antennas to discriminate between signals originating from different communication satellites. With this system, satellites operating on a common frequency band must be spaced at least two degrees of orbit apart. Such a system has a potential of no more than 50 satellites for North American communications. A further restriction results, as these satellites have a limited capability due to their small size. One can conclude that with the above described technology

level, our communication capability is limited to a level far below that which society will demand in the 1990s and beyond.

The future technology of advanced communication systems will utilize satellites with large antennas. Large antennas will focus signals on small Earth spots. This allows the stationing of antennas at less than two degrees of separation. Additionally, these antennas are capable of handling many more communication channels per satellite. Thus, development of large antennas will solve the communications problem well into the future.

In order for these large antennas to function as desired, they must be very large (100m in diameter or larger), and they must possess very accurate reflective surfaces with RMS surface errors less than 7.5mm (2). A popular design of these antennas features the hoop/column concept shown in Figure 1.1.

The hoop/column antenna structure is a cable-tensioned structure. Cable forces are generated by drawing surface control cables toward the bottom of the column. The hoop is forced radially outward by several mechanical springs located in the hoop mechanism. The reflective surface, lower tensioning cords, and surface ties compose a geometrically nonlinear structure.

The purpose of the research reported herein is to determine the optimal tensioning loads for such an antenna. Such

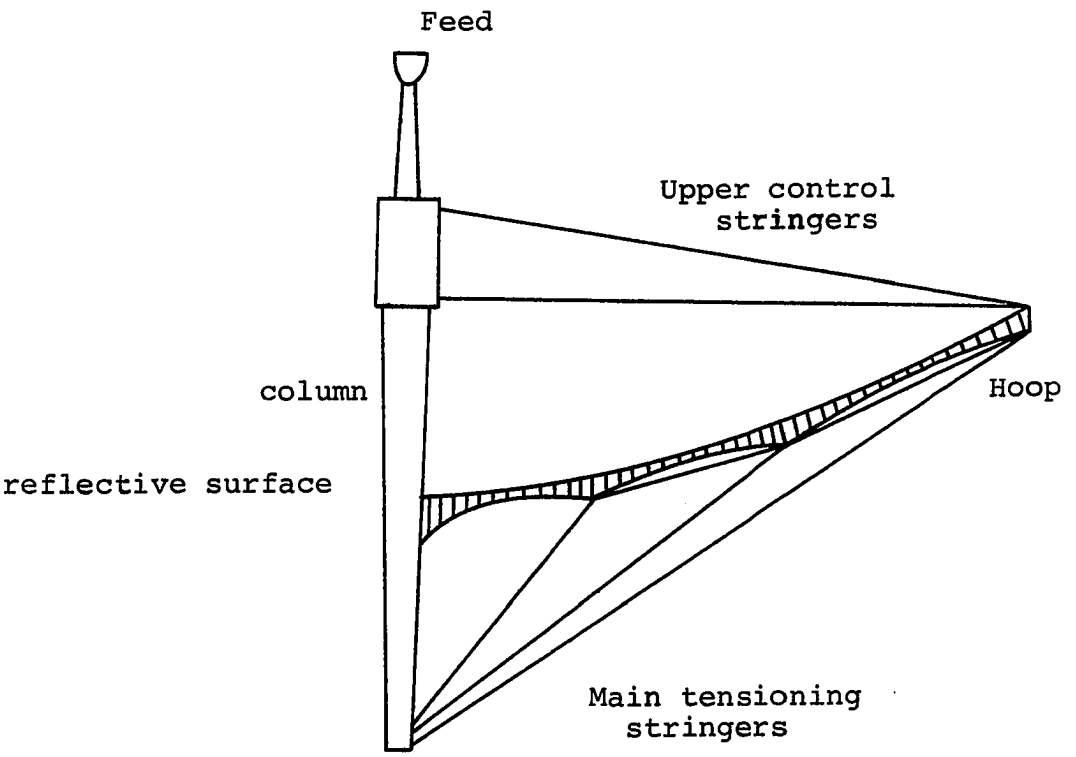

(Note: the antenna is symmetric about the column)

Figure 1.1. Hoop/column antenna cross section

a tool is useful in initially deploying the antenna, in adjusting the tensioning loads when the structure deforms due to thermal loads, and possibly in readjusting the antenna surface should a structural member fail. This problem is represented mathematically as

$$\min \Phi \ (\tilde{R}_{x_1}, \tilde{R}_{y_1}, \tilde{R}_{x_2}, \tilde{R}_{y_2}, \ldots, \tilde{R}_{x_n}, \tilde{R}_{y_n}, u_1, v_1, u_2, v_2, \ldots, u_n, v_n)$$

subject to

$$h_i(\tilde{R}_{x_1}, \tilde{R}_{y_1}, \tilde{R}_{x_2}, \tilde{R}_{y_2}, \ldots, \tilde{R}_{x_n}, \tilde{R}_{y_n}, u_1, v_1, u_2, v_2, \ldots, u_n, v_n) = 0$$

where

Φ is an error function

and

h_i are nonlinear equilibrium equations written for each node in the structure

$\tilde{R}$ is the vector of tensioning forces

u,v is the vector of nodal displacements

Levy and Melosh (3) solved a related problem in which a similar objective function was minimized for a ground based antenna. However, the decision variables in their study were defined to be the sizing of the various structural components in the antenna. A linear-elastic structural model was employed in their effort. In another study, Eldred and Schaechter (4) minimized a performance index which is very similar to the objective function employed in the present study. Their study also employed a linear-elastic structural

model (a simple beam). However, these authors defined the decision variables to be the shaping forces.

This dissertation documents the theoretical development of the optimization problem described above. The development of a nonlinear structural analyzer and the coupling of this analyzer to the optimization algorithm are described. Two-dimensional numerical problems are solved in order to verify the technique. The optimal tensioning loads are determined for each model. Each model is then subjected to a temperature change and the new optimal tensioning loads are determined.

2. THE DESIGN PROBLEM

In any design problem, the goal of the designer is to determine values for those parameters which result in the design performing some function "best". This function, Φ, is often known as the objective function or cost function and this best solution is known as an optimal solution. The parameters, for which values are sought, are known as decision variables. These decision variables define a design space in which to operate.

The well-known necessary and sufficient conditions for this optimum solution of an unconstrained problem require:

$$\nabla\Phi(\chi^*) = 0$$

$$z^T \nabla^2(\chi^*) z \geq 0 \qquad (2.1)$$

If the above equations are satisfied at a point R* in the design space, and if z is a nonzero vector, then Φ has a local minimum at χ^*.

A gradient-type optimization algorithm was employed in the present study. A detailed description of this algorithm is contained in Chapter 4. The solution to the design problem requires both function and gradient information.

Consider the antenna segment as shown in Figure 2.1,

$$\Phi \triangleq \sum_{i=1}^{N} \int_{x_{s_i}}^{x_{s_{i+1}}} (\hat{y}-y)^2 dx \qquad (2.2)$$

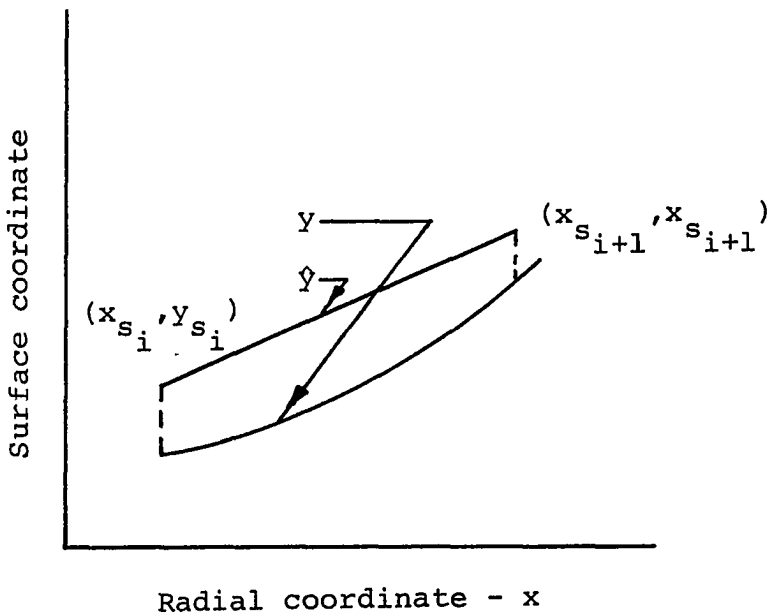

Figure 2.1. j^{th} antenna segment between surface node i and node i+1

The i^{th} surface node is located at the point x_{s_i}, y_{s_i}. There are N straight line segments describing the antenna surface. y is the target antenna shape and is described as the parabola

$$y = Ax^2 + B \tag{2.3}$$

and $\hat{y}$ is the function describing the antenna surface

$$\hat{y} = \frac{y_{s_{i+1}} - y_{s_i}}{x_{s_{i+1}} - x_{s_i}} (x - x_{s_i}) + y_{s_i} \qquad x_{s_i} < x < x_{s_{i+1}} \tag{2.4}$$

The error function can be rewritten as

$$\Phi = \sum_{i=1}^{N} \int_{x_{s_i}}^{x_{s_{i+1}}} [-Ax^2 + \beta x + \gamma]^2 dx \tag{2.5}$$

where

$$\beta \triangleq \frac{y_{s_{i+1}} - y_{s_i}}{x_{s_{i+1}} - x_{s_i}}$$

and

$$\gamma \triangleq y_{s_i} - \beta x_{s_i} - B$$

After integration,

$$\Phi = \sum_{i=1}^{N} \left[\frac{1}{5}A^2 (x_{s_{i+1}}^5 - x_{s_i}^5) - \frac{1}{2}A\beta (x_{s_{i+1}}^4 - x_{s_i}^4) + \frac{1}{3}(\beta^2 - 2A\gamma)(x_{s_{i+1}}^3 - x_{s_i}^3) + \beta\gamma (x_{s_{i+1}}^2 - x_{s_i}^2) + \gamma^2 (x_{s_{i+1}} - x_{s_i})\right] \tag{2.6}$$

In order to determine the tensioning loads which form the optimal shape we must relate Equation 2.6 to the tensioning loads. Consider the motion of a cable in a stationary Cartesian system (Fig. 2.2). We have adopted the standard notation by defining the motion of the body with respect to time. In our case, the "time steps" refer to "load steps". For such analysis

$$ {}^{t}x_i = {}^{o}x_i + {}^{t}u_i \tag{2.7a} $$

$$ {}^{t+\Delta t}x_i = {}^{o}x_i + {}^{t+\Delta t}u_i \tag{2.7b} $$

where i denotes the point of interest. The increments in the displacements from time t to time t+Δt can be written as:

$$ u_i = {}^{t+\Delta t}u_i + {}^{t}u_i \tag{2.8} $$

Similar equations describe the kinematics in the y-direction. The displacements are related to the applied forces by equilibrium equations. The modified Newton-Raphson form of these equations as described by Bathe (5) is

$$ {}^{t+\Delta t}K\,{}^{t+\Delta t}\Delta u = {}^{t+\Delta t}R - {}^{t+\Delta t}F \tag{2.9} $$

where

$$ {}^{t+\Delta t}u = {}^{t}u + \alpha\,{}^{t+\Delta t}\Delta u \tag{2.10} $$

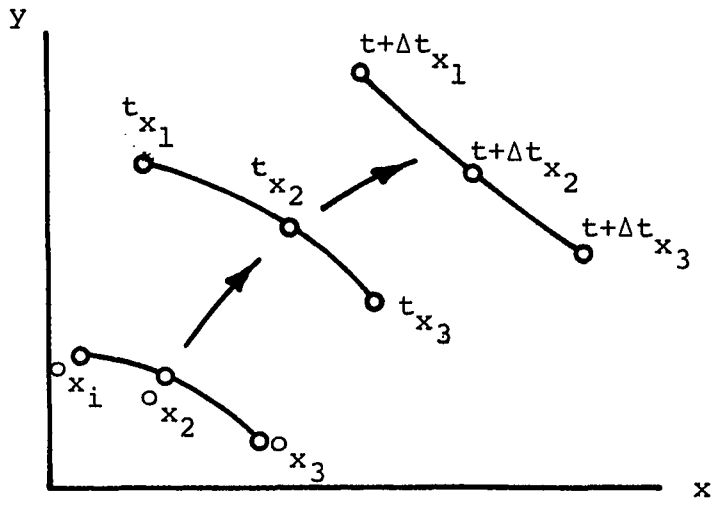

Figure 2.2. Motion of a cable in a Cartesian coordinate system

In these equations, ${}^{t+\Delta t}K$ is the tangent stiffness matrix evaluated at time $t+\Delta t$, ${}^{t+\Delta t}R$ is the vector of nodal loads evaluated at time $t+\Delta t$, and ${}^{t+\Delta t}F$ is the vector of point nodal forces corresponding to elemental stresses at time $t+\Delta t$. Equation 2.9 is solved for ${}^{t+\Delta t}\Delta U$ and the displacements are determined using a numerical technique described in Chapter 3. Equation 2.9 is a set of nonlinear equality constraint equations which must be satisfied if the solution is to be feasible. The algorithm employed in simultaneously satisfying these equations and minimizing the objective function is discussed in Chapter 4.

The gradient of the objective function with respect to nodal forces can be written as:

$$\frac{\partial \Phi}{\partial {}^{t}R_i} = \frac{\partial \Phi}{\partial x_{s_1}} \frac{\partial x_{s_1}}{\partial u_{s_i}} \frac{\partial u_{s_1}}{\partial {}^{t}R_i} + \frac{\partial \Phi}{\partial x_{s_2}} \frac{\partial x_{s_2}}{\partial u_{s_2}} \frac{\partial u_{s_2}}{\partial {}^{t}R_i} + \ldots +$$

$$\frac{\partial \Phi}{\partial x_{s_n}} \frac{\partial x_{s_n}}{\partial u_{s_n}} \frac{\partial u_{s_n}}{\partial {}^{t}R_i} + \frac{\partial \Phi}{\partial y_{s_1}} \frac{\partial y_{s_1}}{\partial v_{s_1}} \frac{\partial v_{s_1}}{\partial {}^{t}R_i}$$

$$\frac{\partial \Phi}{\partial y_{s_2}} \frac{\partial y_{s_2}}{\partial v_{s_2}} \frac{\partial u_{s_2}}{\partial {}^{t}R_i} + \ldots +$$

$$\frac{\partial \Phi}{\partial y_{s_n}} \frac{\partial y_{s_n}}{\partial v_{s_n}} \frac{\partial v_{s_n}}{\partial {}^{t}R_i} \qquad (2.11)$$

The partial derivations of the surface error in the j^{th} surface segment with respect to the surface coordinates are

$$\left(\frac{\partial \Phi}{\partial x_{s_i}}\right) = -A^2 x_{s_i}^4 - \frac{1}{2}A(y_{s_{i+1}} - y_{s_i})(x_{s_{i+1}}^2 + 2x_{s_i} x_{s_{i+1}} + 3x_{s_i}^2)$$

$$+ \frac{1}{3}\left(2\beta\frac{\partial \beta}{\partial x_{s_i}} - 2A\frac{\partial \gamma}{\partial x_{s_i}}\right)(x_{s_{i+1}}^3 - x_{s_i}^3) - (\beta^2 - 2A\gamma)x_{s_i}^2$$

$$- 2x_{s_i}\beta\gamma + (x_{s_{i+1}}^2 - x_{s_i}^2)\left(\gamma\frac{\partial \beta}{\partial x_{s_i}} + \frac{\partial \gamma}{\partial x_{s_i}}\right)$$

$$- \gamma^2 + 2\gamma(x_{s_{i+1}} - x_{s_i})\frac{\partial \gamma}{\partial K_{s_i}} \qquad (2.12a)$$

$$\left(\frac{\partial \Phi}{\partial y_{s_i}}\right)_j = \frac{1}{2}(Ax_{s_{i+1}}^3 + x_{s_i} x_{s_{i+1}}^2 + x_{s_i}^2 x_{s_{i+1}} + x_{s_i}^3)$$

$$+ \frac{1}{3}(x_{s_{i+1}}^3 - x_{s_i}^3)\left(2\beta\frac{\partial \beta}{\partial y_{s_i}} - 2A\frac{\partial \gamma}{\partial y_{s_i}}\right)$$

$$+ (x_{s_{i+1}}^2 - x_{s_i}^2)\left(\gamma\frac{\partial \beta}{\partial y_{s_i}} + \beta\frac{\partial \gamma}{\partial y_{s_i}}\right) + 2\gamma(x_{s_{i+1}} - x_{s_i})\frac{\partial \gamma}{\partial y_{s_i}}$$

(2.12b)

$$\left(\frac{\partial\Phi}{\partial x_{s_{i+1}}}\right)_j = A^2 x_{s_{i+1}}^4 - \frac{1}{2}A(y_{s_{i+1}} - y_{s_i})(3x_{s_{i+1}}^2 + 2x_{s_i}x_{s_{i+1}} + x_{s_i}^2)$$

$$+ \frac{1}{3}\left(2\beta\frac{\partial\beta}{\partial x_{s_{i+1}}} - 2A\frac{\partial\gamma}{\partial x_{s_{i+1}}}\right)(x_{s_{i+1}}^3 - x_{s_i}^3) + (\beta^2 - 2A\gamma)x_{s_{i+1}}^2$$

$$+ 2x_{s_{i+1}}\beta\gamma + (x_{s_{i+1}}^2 - x_{s_i}^2)\left(\gamma\frac{\partial\beta}{\partial x_{s_{i+1}}} + \beta\frac{\partial\gamma}{\partial x_{s_{i+1}}}\right)$$

$$+ \gamma^2 + 2\gamma(x_{s_{i+1}} - x_{s_i})\frac{\partial\gamma}{\partial x_{s_{i+1}}} \qquad (2.12c)$$

$$\left(\frac{\partial\Phi}{\partial y_{s_{i+1}}}\right)_j = -\frac{1}{2}A(x_{s_{i+1}}^3 + x_{s_i}x_{s_{i+1}}^2 + x_{s_i}x_{s_{i+1}}^2 + x_{s_i}^3)$$

$$+ \frac{1}{3}(x_{s_{i+1}}^3 - x_{s_i}^3)\left(2\beta\frac{\partial\beta}{\partial y_{s_{i+1}}} - 2A\frac{\partial\gamma}{\partial y_{s_{i+1}}}\right)$$

$$+ (x_{s_{i+1}}^2 - x_{s_i}^2)\left(\gamma\frac{\partial\beta}{\partial y_{s_{i+1}}} + \beta\frac{\partial\gamma}{\partial y_{s_{i+1}}}\right)$$

$$+ 2\gamma(x_{s_{i+1}} - x_{s_i})\frac{\partial\gamma}{\partial y_{s_{i+1}}} \qquad (2.12d)$$

where

$$\frac{\partial\beta}{\partial k_{s_i}} = (y_{s_{i+1}} - y_{s_i})(x_{s_{i+1}} - x_{s_i})^{-2} \qquad (2.12e)$$

$$\frac{\partial\gamma}{\partial x_{s_i}} = -\beta - x_{s_i}\frac{\partial\beta}{\partial x_{s_i}} \qquad (2.12f)$$

$$\frac{\partial\beta}{\partial y_{s_i}} = -(x_{s_{i+1}} - x_{s_i})^{-1} \qquad (2.12g)$$

$$\frac{\partial \gamma}{\partial y_{s_i}} = 1 - x_{s_i} \frac{\partial \beta}{\partial y_{s_i}} \tag{2.12h}$$

$$\frac{\partial \beta}{\partial x_{s_{i+1}}} = -(y_{s_{i+1}} - y_{s_i})(x_{s_{i+1}} - x_{s_i})^{-2} \tag{2.12i}$$

$$\frac{\partial \gamma}{\partial x_{s_{i+1}}} = -x_{s_i} \frac{\partial \beta}{\partial x_{s_{i+1}}} \tag{2.12j}$$

The gradient terms above are the contribution for a single antenna segment. Adjacent antenna segments each contribute to the gradient terms corresponding to the node between the segments (refer to Figure 2.3). Hence,

$$\begin{Bmatrix} \frac{\partial \Phi}{\partial x_{s_k}} \\ \\ \frac{\partial \Phi}{\partial y_{s_k}} \end{Bmatrix} = \begin{Bmatrix} (\frac{\partial \Phi}{\partial x_{s_{i+1}}})_j \\ \\ (\frac{\partial \Phi}{\partial y_{s_{i+1}}})_j \end{Bmatrix} + \begin{Bmatrix} (\frac{\partial \Phi}{\partial x_{s_i}})_{j+1} \\ \\ (\frac{\partial \Phi}{\partial y_{s_i}})_{j+1} \end{Bmatrix} \tag{2.13}$$

In this equation, the index i denotes a local node number and the index k denotes a global node number. Hence, $(\frac{\partial \Phi}{\partial x_{s_{i+1}}})_j$ corresponds to $i+1^{th}$ (right hand) node of the j^{th} surface segment. The term $(\frac{\partial \Phi}{\partial x_{s_i}})_{j+1}$ corresponds to the i^{th} (left hand) node of the j+1 surface segment.

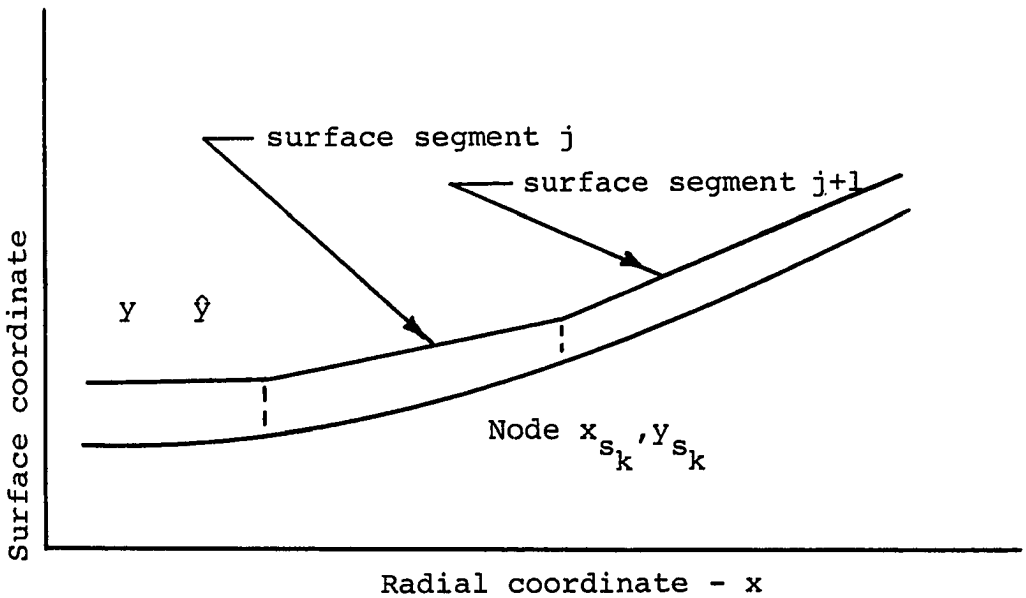

Figure 2.3. Antenna surface geometry

Examining Equations 2.7, it is obvious that

$$\frac{\partial x_{s_i}}{\partial u_i} = 1 \tag{2.14}$$

If we limit the optimization algorithm such that only small changes occur in the applied load, then it can be assumed that ${}^{t+\Delta t}\{F\}$ in Equation 2.9 is constant. Since our next load step is close to the equilibrium condition, we will assume that $\alpha=1$. This last assumption is a reversion to the standard Newton-Raphson form of the nonlinear finite element equations. These assumptions yield the equation

$${}^{t+\Delta t}[K]\{\Delta u\} = {}^{t+\Delta t}\{R-F\} \tag{2.15}$$

or

$${}^{t+\Delta t}[K]\{{}^{t+\Delta t}u - {}^{t}u\} = {}^{t+\Delta t}\{R-F\} \tag{2.16}$$

$$\{{}^{t+\Delta t}u - {}^{t}u\} = {}^{t+\Delta t}[K]^{-1}\ {}^{t+\Delta t}\{R-F\} \tag{2.17}$$

$${}^{t+\Delta t}\{u\} = {}^{t+\Delta t}[K]^{-1}\ {}^{t+\Delta t}\{R\} - {}^{t+\Delta t}[K]^{-1}\ {}^{t+\Delta t}\{F\} + {}^{t}\{u\}$$

therefore (2.18)

$$\frac{\partial {}^{t+\Delta t}u_i}{\partial {}^{t+\Delta t}R_j} = {}^{t+\Delta t}K^{-1}_{ij} \tag{2.19}$$

Equation 2.19 is to be interpreted as the i,j element of the inverse stiffness matrix at time $t+\Delta t$.

At this point, we can completely evaluate $\frac{\partial \Phi}{\partial R_i}$ where R_i is an applied nodal force along the global axis.

The geometry of a typical antenna design is shown in Figure 2.4.

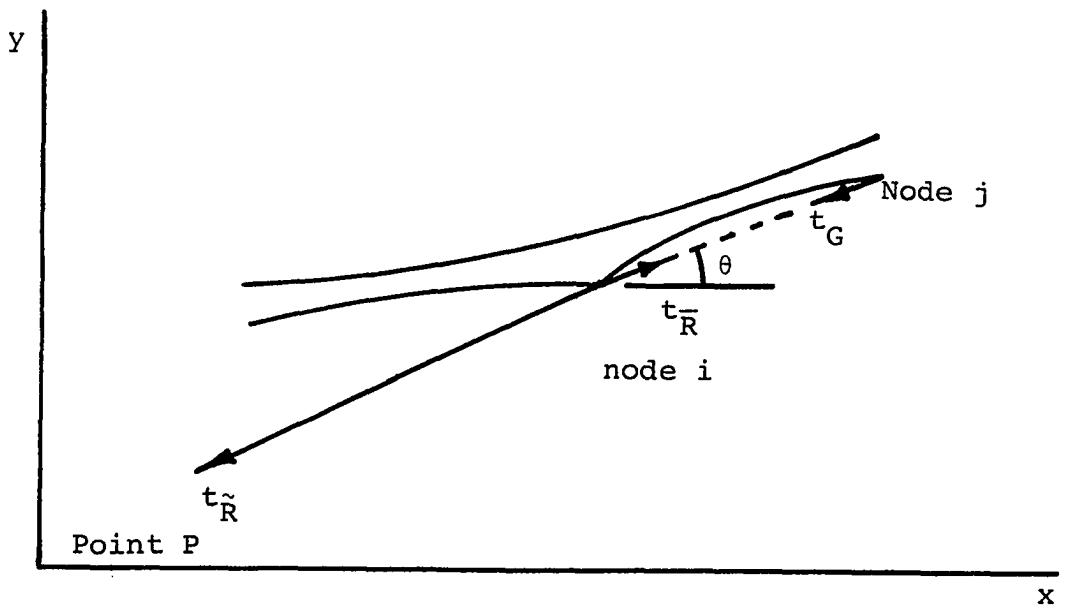

Figure 2.4. Antenna tensioning force geometry

The force system shown in Figure 2.4 represents a lower surface tensioning cable. This cable is attached to the antenna rib at node j, passes over a frictionless pulley at node i, and is drawn toward the column at point P. Note that $t_{\tilde{R}}$ is a nonlinear force which rotates as the structure deforms. Force $t_{\tilde{R}}$ always acts toward point P. Since a frictionless pulley is located at node i, the forces $t_{\bar{R}}$

and ${}^{t}G$ are equal in magnitude to force ${}^{t}\tilde{R}$. These forces act in the directions shown in Figure 2.4.

At node i, the applied nodal force vector is given by:

$$ {}^{t}\begin{Bmatrix} R_{x_i} \\ R_{y_i} \end{Bmatrix} = \begin{Bmatrix} (\cos\theta)\ {}^{t}\tilde{R}_x^2 + {}^{t}\tilde{R}_y^2 + {}^{t}\tilde{R}_x \\ (\sin\theta)\ {}^{t}\tilde{R}_x^2 + {}^{t}\tilde{R}_y^2 + {}^{t}\tilde{R}_y \end{Bmatrix} \qquad (2.20) $$

At node j, the applied nodal force vector is given by:

$$ {}^{t}\begin{Bmatrix} R_{x_j} \\ R_{y_j} \end{Bmatrix} = \begin{Bmatrix} -(\cos\theta)\ {}^{t}\tilde{R}_x^2 + {}^{t}\tilde{R}_y^2 \\ -(\sin\theta)\ {}^{t}\tilde{R}_x^2 + {}^{t}\tilde{R}_y^2 \end{Bmatrix} \qquad (2.21) $$

The gradient of the objective function in terms of the components of ${}^{t}\tilde{R}$ is given by:

$$ \frac{\partial\Phi}{\partial {}^{t}\tilde{R}_{x_i}} = \frac{\partial\Phi}{\partial {}^{t}R_{x_i}} \frac{\partial R_{x_i}}{\partial {}^{t}\tilde{R}_{x_i}} + \frac{\partial\Phi}{\partial {}^{t}R_{y_i}} \frac{\partial {}^{t}R_{y_i}}{\partial {}^{t}\tilde{R}_{x_i}} + $$

$$ + \frac{\partial\Phi}{\partial {}^{t}G_{x_j}} \frac{\partial {}^{t}G_{x_j}}{\partial {}^{t}\tilde{R}_{x_i}} + \frac{\partial\Phi}{\partial {}^{t}G_{y_i}} \frac{\partial {}^{t}G_{y_i}}{\partial {}^{t}\tilde{R}_{x_i}} \qquad (2.22a) $$

$$ \frac{\partial\Phi}{\partial {}^{t}\tilde{R}_{y_i}} = \frac{\partial\Phi}{\partial {}^{t}R_{x_i}} \frac{\partial {}^{t}R_{x_i}}{\partial {}^{t}\tilde{R}_{y_i}} + \frac{\partial\Phi}{\partial {}^{t}R_{y_i}} \frac{\partial {}^{t}R_{y_i}}{\partial {}^{t}\tilde{R}_{y_i}} + \frac{\partial\Phi}{\partial {}^{t}G_{x_j}} \frac{\partial {}^{t}G_{x_j}}{\partial {}^{t}\tilde{R}_{y_i}} $$

$$ + \frac{\partial\Phi}{\partial {}^{t}G_{y_i}} \frac{\partial {}^{t}G_{y_j}}{\partial {}^{t}\tilde{R}_{y_i}} \qquad (2.22b) $$

where

$$\frac{\partial {}^{t}R_{x_i}}{\partial {}^{t}\tilde{R}_{x_i}} = {}^{t}\tilde{R}_{x_i}\left[{}^{t}\tilde{R}_{x_i}^{2} + {}^{t}\tilde{R}_{y_i}\right]^{-\frac{1}{2}} \cos\theta + 1 \qquad (2.23a)$$

$$\frac{\partial {}^{t}R_{y_i}}{\partial {}^{t}\tilde{R}_{x_i}} = {}^{t}\tilde{R}_{x_i}\left[{}^{t}\tilde{R}_{x_i}^{2} + {}^{t}\tilde{R}_{y_i}^{2}\right]^{-\frac{1}{2}} \sin\theta \qquad (2.23b)$$

$$\frac{\partial {}^{t}R_{y_i}}{\partial {}^{t}\tilde{R}_{y_i}} = {}^{t}\tilde{R}_{y_i}\left[{}^{t}\tilde{R}_{x_i}^{2} + {}^{t}\tilde{R}_{y_i}^{2}\right]^{-\frac{1}{2}} \cos\theta \qquad (2.23c)$$

$$\frac{\partial {}^{t}R_{y_i}}{\partial {}^{t}\tilde{R}_{y_i}} = {}^{t}\tilde{R}_{y_i}\left[{}^{t}\tilde{R}_{x_i}^{2} + {}^{t}\tilde{R}_{y_i}^{2}\right]^{-\frac{1}{2}} \sin\theta + 1 \qquad (2.23d)$$

Recall that the vector $\frac{\partial \Phi}{\partial {}^{t}R_i}$ is given by Equation 2.11, and

$$\frac{\partial {}^{t}G_{s_j}}{\partial {}^{t}\tilde{R}_{x_i}} = {}^{t}\tilde{R}_{x_i}\left[{}^{t}\tilde{R}_{x_i}^{2} + {}^{t}\tilde{R}_{y_i}^{2}\right]^{-\frac{1}{2}} \cos\theta \qquad (2.24a)$$

$$\frac{\partial {}^{t}G_{y_j}}{\partial {}^{t}\tilde{R}_{x_i}} = {}^{t}\tilde{R}_{x_i}\left[{}^{t}\tilde{R}_{x_i}^{2} + {}^{t}\tilde{R}_{y_i}^{2}\right]^{-\frac{1}{2}} \sin\theta \qquad (2.24b)$$

$$\frac{\partial {}^{t}G_{x_j}}{\partial {}^{t}\tilde{R}_{y_i}} = {}^{t}\tilde{R}_{y_i}\left[{}^{t}\tilde{R}_{x_i}^{2} + {}^{t}\tilde{R}_{y_i}^{2}\right]^{-\frac{1}{2}} \cos\theta \qquad (2.24c)$$

$$\frac{\partial {}^{t}G_{y_j}}{\partial {}^{t}\tilde{R}_{y_i}} = {}^{t}\tilde{R}_{y_i}\left[{}^{t}\tilde{R}_{x_i}^{2} + {}^{t}\tilde{R}_{y_i}^{2}\right]^{-\frac{1}{2}} \sin\theta \qquad (2.24d)$$

It is desirable that ${}^{t}\tilde{R}$ act toward the lower mast. A change of variables which enforces this condition is defined as

$${}^{t}\tilde{R}_{x_i} = -\chi_i^{2} \qquad (2.25)$$

The new gradient vector becomes

$$\frac{\partial \Phi}{\partial \chi_i} = \frac{\partial \Phi}{\partial {}^{t}\tilde{R}_{x_i}} \frac{\partial {}^{t}\tilde{R}_{x_i}}{\partial \chi_i} \qquad (2.26a)$$

$$= -2\chi_i \frac{\partial \Phi}{\partial {}^{t}\tilde{R}_{x_i}} \qquad (2.26b)$$

3. THE FINITE ELEMENT ANALYSIS

The standard finite element analysis is limited to small strains and small displacements. Any strain below the strain at which the material yields is considered a small strain. A structure exhibits small displacements when there is no significant change in geometry before and after cording.

The hoop/column antenna structure studied in this investigation exhibits geometric nonlinearities. A simple example of such a structure is shown in Figure 3.1. This figure shows a cable which is fixed at both ends and loaded as shown. This cable cannot be analyzed using a linear finite

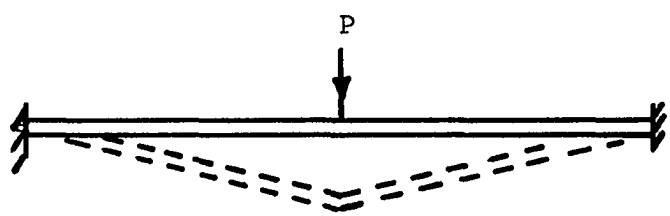

Figure 3.1. Physical example of a geometric nonlinearity

element analysis since the elastic stiffness matrix is singular. The externally applied load P will generate a large rotation before it is reacted by the structure. Such structures are identified as geometrically nonlinear structures. These structures exhibit small strains but large displacements.

Consider the cable element shown in Figure 3.2.

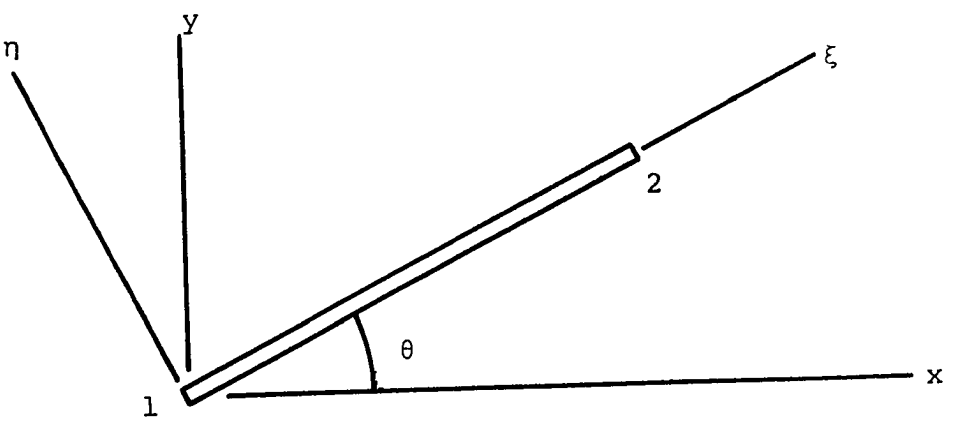

Figure 3.2. Truss element

Adopting the notation of Bathe (5) and Bathe, Ozdemir, and Wilson (6) for this type of problem, the strain displacement relation for such an element is given by the equation

$$ {}^{t}\varepsilon_{\xi\xi} = \frac{\partial {}^{t}u}{\partial \xi} + \frac{1}{2}\left[\left(\frac{\partial {}^{t}u}{\partial \xi}\right)^2 + \left(\frac{\partial {}^{t}v}{\partial \xi}\right)^2\right] \tag{3.1} $$

Assuming a linear displacement field in the element coordinate system yields

$$ {}^{t}u = \left(1 - \frac{\xi}{2}\right){}^{t}u_1 + \left(\frac{\xi}{2}\right){}^{t}u_2 \tag{3.2a} $$

$$ {}^{t}v = \left(1 - \frac{\xi}{2}\right){}^{t}v_1 + \left(\frac{\xi}{2}\right){}^{t}v_2 \tag{3.2b} $$

Substituting Equation 3.2a into the first term of Equation 3.1 yields

$$ \frac{\partial {}^{t}u}{\partial \xi} = \begin{bmatrix} L & -\frac{1}{t_L} & 0 & \frac{1}{t_L} & 0 \end{bmatrix} \begin{Bmatrix} {}^{t}u_1 \\ {}^{t}v_1 \\ {}^{t}u_2 \\ {}^{t}v_2 \end{Bmatrix} \tag{3.3} $$

$$ = [B]\{u\} \tag{3.4} $$

$$ [K_e] = \int_{vol} [B]^T [D] [B] dV \tag{3.5} $$

where D is the material matrix, or in our case, simply Young's modulus E. Performing the above integration yields the elastic stiffness material for a truss element.

$$[K_e] = \frac{AE}{t_L}\begin{bmatrix} 1 & 0 & -1 & 0 \\ 0 & 0 & 0 & 0 \\ -1 & 0 & 1 & 0 \\ 0 & 0 & 0 & 0 \end{bmatrix} \tag{3.6}$$

The second term of Equation 3.1 can be written as

$$\frac{1}{2}\{{}^{t}u\}[B_{NL}]^{T}[B_{NL}]\{{}^{t}u\}$$

where

$$\begin{Bmatrix} \frac{\partial {}^{t}u}{\partial \xi} \\ \frac{\partial {}^{t}v}{\partial \xi} \end{Bmatrix} = \frac{1}{t_L}\begin{bmatrix} -1 & 0 & 1 & 0 \\ 0 & -1 & 0 & 1 \end{bmatrix}\begin{Bmatrix} {}^{t}u_1 \\ {}^{t}v_1 \\ {}^{t}u_2 \\ {}^{t}v_2 \end{Bmatrix} \tag{3.7}$$

$$= [B_{NL}]\{{}^{t}u\} \tag{3.8}$$

Again, adopting standard form

$$[K_{NL}] = \int_{vol} [B_{NL}]^{T}[D_{NL}][B_{NL}]dV \tag{3.9}$$

where $[D_{NL}]$ for an axial stiffness element is simply the axial stress at time multiplied by the identity matrix. For a uniform element of constant cross section, the stress will be constant throughout the element. Therefore, Equation 3.9 yields

$$[K_{NL}] = \frac{t_{\tau A}}{t_L} \begin{bmatrix} 1 & 0 & -1 & 0 \\ 0 & 1 & 0 & -1 \\ -1 & 0 & 1 & 0 \\ 0 & -1 & 0 & 1 \end{bmatrix} \tag{3.10}$$

$$[K_{NL}] = \frac{t_P}{t_L} \begin{bmatrix} 1 & 0 & -1 & 0 \\ 0 & 1 & 0 & -1 \\ -1 & 0 & 1 & 0 \\ 0 & -1 & 0 & 1 \end{bmatrix} \tag{3.11}$$

where the Cauchy stress $^{t}\tau$ is given by

$$^{t}\tau = E\frac{t_L - o_L}{L_o} + \frac{1}{2}E\,\bar{\alpha}\Delta T \tag{3.12}$$

where $\bar{\alpha}$ is the coefficient of thermal expansion and ΔT is the element temperature change. Assembly of these matrices into the global stiffness matrix is performed in the usual way. The elemental stiffness matrices are first transformed into global coordinates after which they are assembled in a manner consistent with integration over the entire domain in an element by element fashion

$$[K_{GL}] = [T]^T [K] [T] \tag{3.13}$$

where

$$[T] = \begin{bmatrix} \cos\theta & \sin\theta & 0 & 0 \\ -\sin\theta & \cos\theta & 0 & 0 \\ 0 & 0 & \cos\theta & \sin\theta \\ 0 & 0 & -\sin\theta & \cos\theta \end{bmatrix} \tag{3.14}$$

Due to the form of Equation 3.11, $[K_{NL}]$ in local coordinates is identical to $[K_{NL}]$ in global coordinates.

The development of stiffness matrices is now complete. Note that the geometric nonlinearity influences the matrices in several ways. The finite element equations (Equation 2.4) are functions of the current geometry (i.e., the geometry at time $t+\Delta t$). The current geometry controls both direction cosines and the current element length.

As indicated in the previous chapter, the modified Newton-Raphson form of the assembled finite element equations are

$$^{t+\Delta t}K\,{}^{t+\Delta t}\Delta u = {}^{t+\Delta t}R - {}^{t+\Delta t}F \tag{2.9}$$

where

$$^{t+\Delta t}u = {}^{t}u + \alpha\,{}^{t+\Delta t}\Delta u \tag{2.10}$$

Recall that $^{t+\Delta t}R$ is the vector of applied loads at time t+ t and $^{t+\Delta t}F$ is the vector of point nodal forces corresponding to elemental stresses at time $t+\Delta t$. For an antenna analysis, the vector $^{t+\Delta t}R$ contains a cable

force which is oriented toward a particular point or node. Therefore, these forces rotate as the structure deforms. ${}^{t+\Delta t}R$ also contains components due to thermal loads. The governing finite element equations possess geometric nonlinearities in the stiffness matrix, the applied load vector, and in the vector of point nodal forces. Solution of the nonlinear finite element problem starts with the assembly of the stiffness matrix and the force imbalance vector. Equation 2.9 is then solved for ${}^{t+\Delta t}\Delta u$. The step size α contained in Equation 2.10 is then determined using the following iterative scheme. For a given α, one can compute the following inner product between the current search direction and the current force imbalance vector.

$$ {}^{t+\Delta t}\Delta u^{T}\{{}^{t+\Delta t}R - {}^{t+\Delta t}F\} \qquad (3.16) $$

Note that both ${}^{t+\Delta t}R$ and ${}^{t+\Delta t}F$ are functions of the stepsize α.

The value of α is selected such that this inner product is sufficiently close to zero. A fixed point iteration scheme is used for this operation. A limitation is imposed on alpha, restricting its value to be less than or equal to one. This technique for determining the stepsize is included in the BFGS (Broyden-Fletcher-Goldfarb-Shannon) method for solving nonlinear finite element equations as reported by Bathe and Cimento (7).

Due to the sensitivity of the equations used to model an antenna, α was determined precisely in this analysis. Other investigators have successfully used less precise values

for α while analyzing different problems (5).

After determining a value for α, the coordinates are updated using Equation 2.10. The process is now repeated starting with the reformulation of the stiffness matrix. The convergence criteria for this iterative procedure is a check on the norm of the force imbalance vector.

A typical antenna rib geometry is shown in Figure 3.3. It is apparent by inspection that the elastic stiffness matrix of this structure is singular. It is therefore

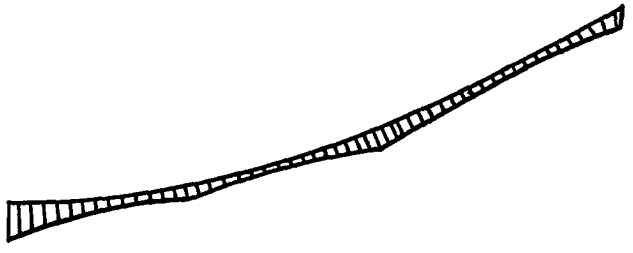

Figure 3.3. Typical antenna rib

necessary to make a reasonable estimate of the displacements in order to initiate the solution process. A poor estimate will result in either a nonpositive definite stiffness matrix or in unacceptably high nodal point forces due to elemental stresses which result in a very large force imbalance vector. This latter condition can result in excessive solution times or divergence of the solution altogether.

4. THE OPTIMIZATION ALGORITHM

A modified conjugate gradient algorithm was employed in this study. Recall that the conjugate gradient method can be used to minimize an unconstrained function by generating a sequence of moves from an initial point χ^0 to a new point χ^1 and so on. Each new point is described by the relation

$$\chi^k = \chi^{k-1} + \alpha_k^* z^k \tag{4.1}$$

where

z^k is the direction of search

χ^{k-1} is the current point

χ^k is the new point

and

α_k^* is the optimum step size

The initial search direction is a steepest descent step

$$z^1 = - \nabla\Phi(\chi^0). \tag{4.2}$$

This step is followed by n-1 conjugate gradient steps

$$z^{k+1} = -\nabla\Phi(\chi^k) + \frac{(\nabla\Phi(\chi^k))^T \nabla\Phi(\chi^k)}{(\nabla\Phi(\chi^{k-1}))^T (\nabla\Phi(\chi^{k-1}))} z^k$$

$$k = 1,\ldots,n-1 \tag{4.3}$$

The optimum step size α_k^* is determined by approximating the objective function along the search direction as a cubic polynomial. Note that if $\Phi(\chi^k)$ is a convex function, then only one relative minimum lies along the search direction.

In the present study, the antenna error Φ is to be minimized while satisfying the equilibrium equations at each node. The conjugate gradient method was modified to solve this particular problem in the following way.

At the initial point, χ^0, a finite element analysis is performed, establishing equilibrium at this point. The tangent stiffness matrix is then inverted, and held constant for the optimization steps. After each one-dimensional minimization, the force imbalance vector is computed. If

$$((R^{t+\ t} - F^{t+\ t})^T\ (R^{t+\ t} - F^{t+\ t})) \leq \varepsilon \qquad (4.4)$$

the method continues as a standard conjugate gradient method. If Equation 4.4 is not satisfied, α^* is halved and Equation 4.4 is checked again. This process is repeated a finite number of times. Since the conjugate gradient method requires accurate one-dimensional minimizations, the optimization process must be restarted from the beginning if α^* is halved. Thus, χ^n becomes χ^0 and the process is repeated starting with another finite element analysis followed by a steepest descent step. This entire process is documented in Figure 4.1.

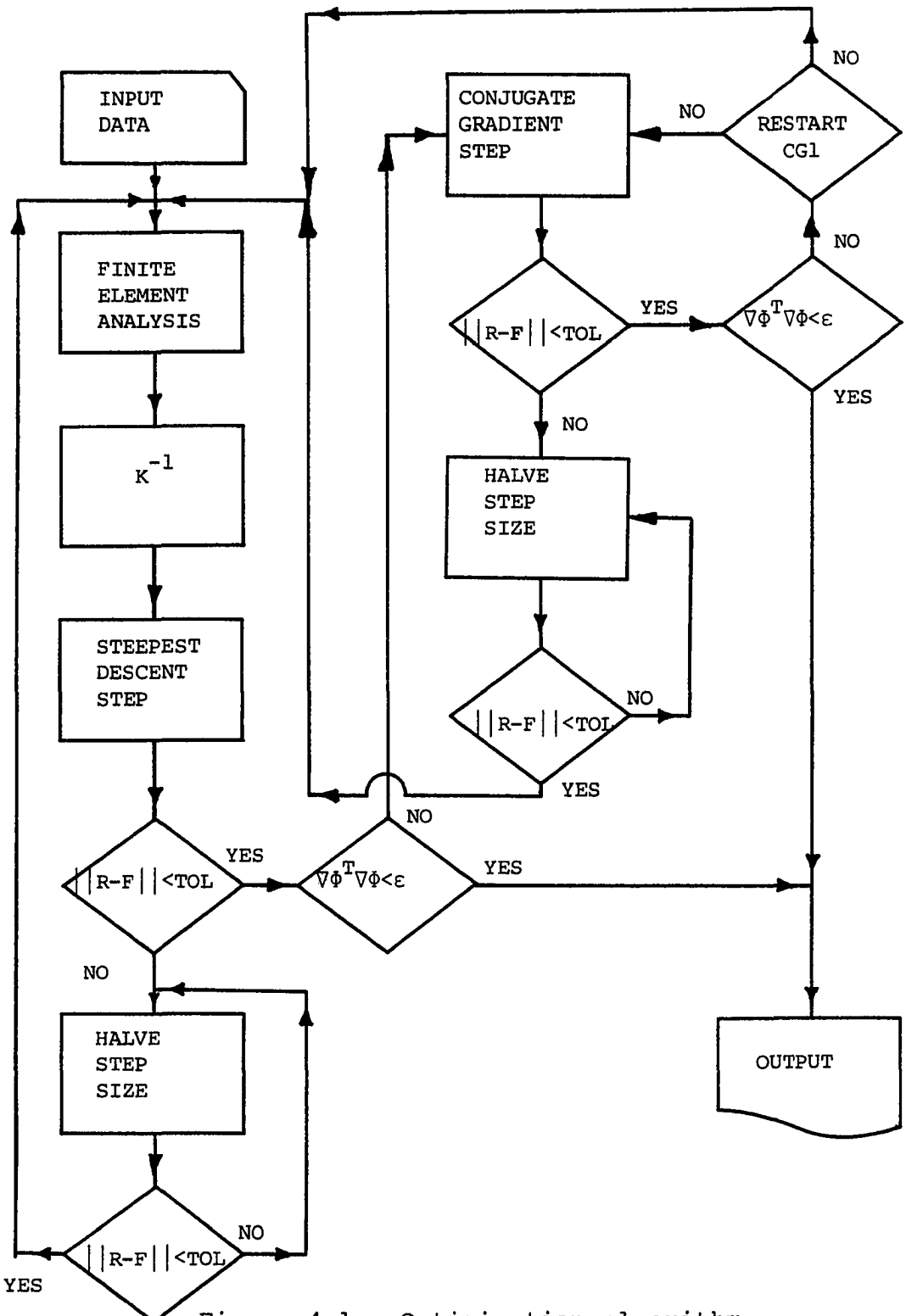

Figure 4.1. Optimization algorithm

5. RESULTS

The optimization algorithm was applied to two antenna rib models. The optimal tensioning loads were determined at various temperatures for each model.

The first model is shown in Figure 5.1. Node numbers and element numbers are shown in this figure. The node numbers are enclosed in circles. The tensioning cable is also shown. It passes over a frictionless pulley located at node 6. The initial coordinates are shown below in Table 5.1.

Table 5.1. Initial nodal coordinates for model 1

Node[a]	X	Y
1	0.0000	-0.0208
2	0.0000	-1.2000
3	5.5400	-0.2840
4	5.7130	-1.0710
5	10.6802	-0.2210
6	10.9344	-1.3580
7	15.5600	0.8245
8	15.7820	0.2830
9	20.0000	1.9788
10	20.0000	1.6000

[a]Nodes 1, 2, 9, and 10 are completely constrained.

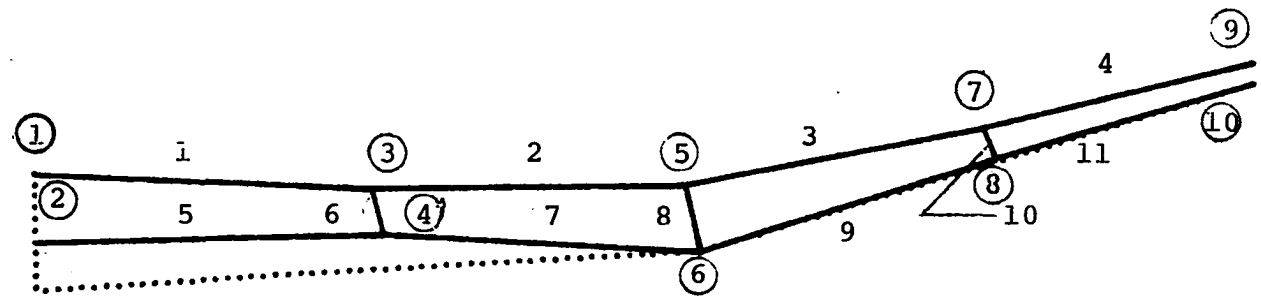

Figure 5.1. Model 1 undeformed geometry

All elements in the rib have the following properties:

$A = 0.1 \text{ in}^2$

$E = 1.25\ (10)^7 \text{ lb/in}^2$

$\alpha = -4.0(10)^{-7} \text{ in/in/°F}$

The optimal tensioning loads were determined for target parabola $\hat{y} = 0.0002\ X^2$. The results of these runs are contained in Tables 5.2-5.4 which summarize the convergence histories for the temperatures indicated.

The deformed and undeformed structural shapes are shown in Figures 5.2-5.4 for the optimal tensioning loads at the temperature indicated. The displacements were increased by a factor of 10.0 for these figures. The function $y-\hat{y}$ is shown in Figures 5.5-5.7. This function is also plotted for the best geometric fit (ref. APPA) in Figure 5.8.

The second antenna rib model is shown in Figure 5.9. Node numbers and element numbers are shown in this figure. The node numbers are enclosed in circles. The tensioning cable is shown passing over a frictionless pulley located at node 6. The initial coordinates are shown below in Table 5.5. All elements in the rib have the following properties:

$A = 0.1 \text{ in}^2$

$E = 1.25\ (10)^7 \text{ lb/in}^2$

$\alpha = 2.0\ (10)^{-6} \text{ in/in/°F}$

Table 5.2. Optimization history, Model 1, $\Delta T = -200°F$[a]

Iteration	X_1	X_1	$\frac{\partial \Phi}{\partial X_1}$	$\frac{\partial \Phi}{\partial X_2}$	Φ
1	10.0	10.0	$-1.032(10)^{-2}$	$8.403(10)^{-3}$	10.007
5	12.115	7.995	$-6.627(10)^{-4}$	$-5.361(10)^{-4}$	9.978
10	12.426	7.552	$-3.685(10)^{-3}$	$5.789(10)^{-3}$	9.972
15	12.575	7.313	$-7.339(10)^{-5}$	$-4.396(10)^{-5}$	9.970
20	12.606	7.261	$-3.141(10)^{-3}$	$5.419(10)^{-3}$	9.969
25	12.622	7.233	$-8.790(10)^{-6}$	$-5.045(10)^{-6}$	9.969
30	12.625	7.226	$-2.894(10)^{-6}$	$-5.051(10)^{-6}$	9.969
35	12.627	7.223	$-1.476(10)^{-6}$	$-8.452(10)^{-7}$	9.969
41	12.628	7.222	$-5.641(10)^{-7}$	$-3.227(10)^{-7}$	9.969

[a]The maximum force imbalance for any degree of freedom is $-7.159\ (10)^{-6}$ lb at the solution. The solution required 114 function evaluations.

Table 5.3. Optimization history, Model 1, $\Delta T = 0°F$[a]

Iteration	X_1	X_2	$\frac{\partial \Phi}{\partial X_1}$	$\frac{\partial \Phi}{\partial X_2}$	Φ
0	10.0	10.0	$-1.029(10)^{-2}$	$8.158(10)^{-3}$	10.016
5	12.117	8.043	$-7.117(10)^{-4}$	$-5.908(10)^{-4}$	9.987
10	12.439	7.595	$-3.622(10)^{-3}$	$5.601(10)^{-3}$	9.981
15	12.599	7.392	$-8.840(10)^{-5}$	$-5.345(10)^{-5}$	9.979
20	12.634	7.282	$-3.020(10)^{-7}$	$5.193(10)^{-3}$	9.979
25	12.654	7.248	$-1.186(10)^{-5}$	$-6.820(10)^{-6}$	9.979
30	12.658	7.240	$-2.885(10)^{-3}$	$5.038(10)^{-3}$	9.979
35	12.661	7.236	$-1.851(10)^{-6}$	$-1.059(10)^{-6}$	9.979
40	12.662	7.235	$-2.331(10)^{-3}$	$4.077(10)^{-3}$	9.979
41	12.662	7.235	$-7.490(10)^{-7}$	$-4.282(10)^{-7}$	9.979

[a]The maximum force imbalance for any degree of freedom is $-8.788(10)^{-6}$ lb at the solution. The solution required 112 function evaluations.

Table 5.4. Optimization history, Model 1, T = +300°F[a]

Iteration	X_1	X_2	$\frac{\partial \Phi}{\partial X_1}$	$\frac{\partial \Phi}{\partial X_2}$	Φ
0	10.000	10.000	$-1.025(10)^{-2}$	$7.756(10)^{-3}$	10.030
5	12.122	8.123	$-7.916(10)^{-4}$	$-6.872(10)^{-4}$	10.003
10	12.461	7.670	$-3.518(10)^{-3}$	$5.273(10)^{-3}$	9.997
15	12.639	7.394	$-1.182(10)^{-4}$	$-7.288(10)^{-5}$	9.995
20	12.682	7.323	$-2.841(10)^{-3}$	$4.848(10)^{-3}$	9.995
25	12.708	7.279	$-1.909(10)^{-5}$	$-1.103(10)^{-5}$	9.994
30	12.714	7.267	$-2.679(10)^{-3}$	$4.671(10)^{-3}$	9.994
35	12.718	7.260	$-3.322(10)^{-6}$	$-1.899(10)^{-6}$	9.994
36	12.719	7.259	$-2.444(10)^{-3}$	$4.278(10)^{-3}$	9.994

[a]The maximum force imbalance for any degree of freedom is $2.45(10)^{-8}$ lb at the solution. The solution required 105 function evaluations.

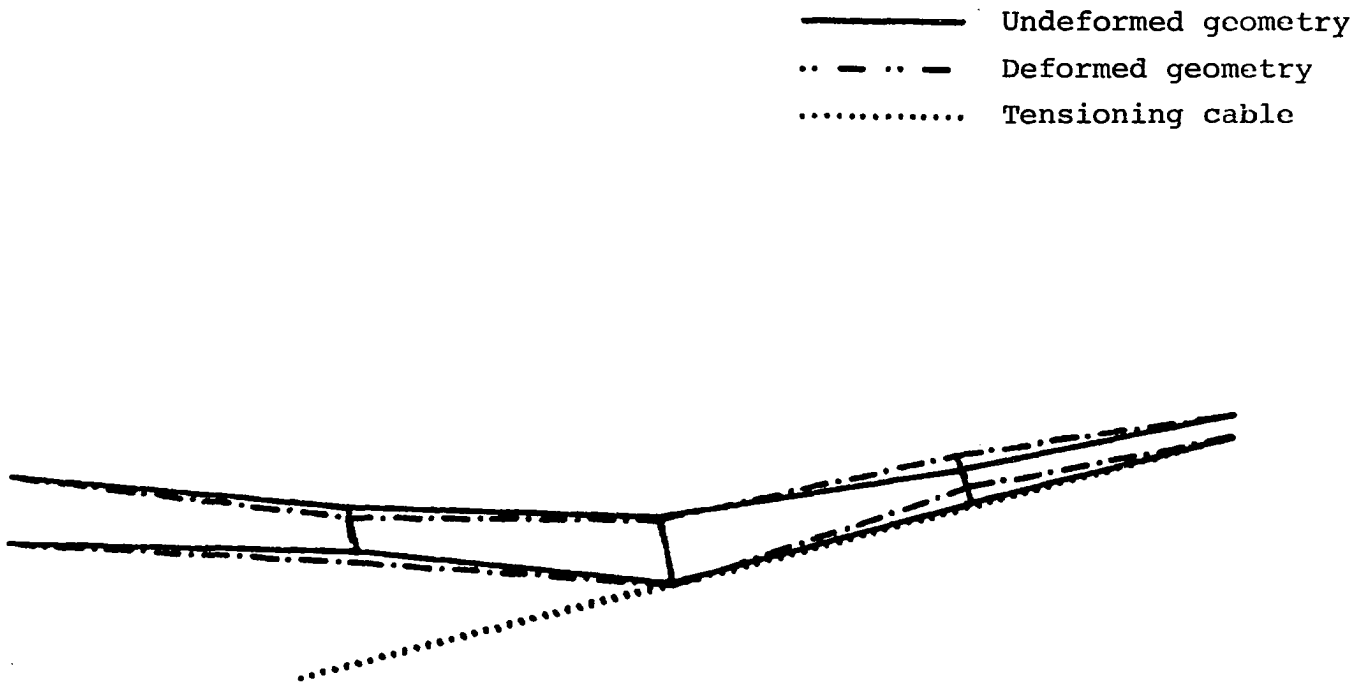

Figure 5.2. Model 1 deformed geometry, $\Delta T = -200°F$

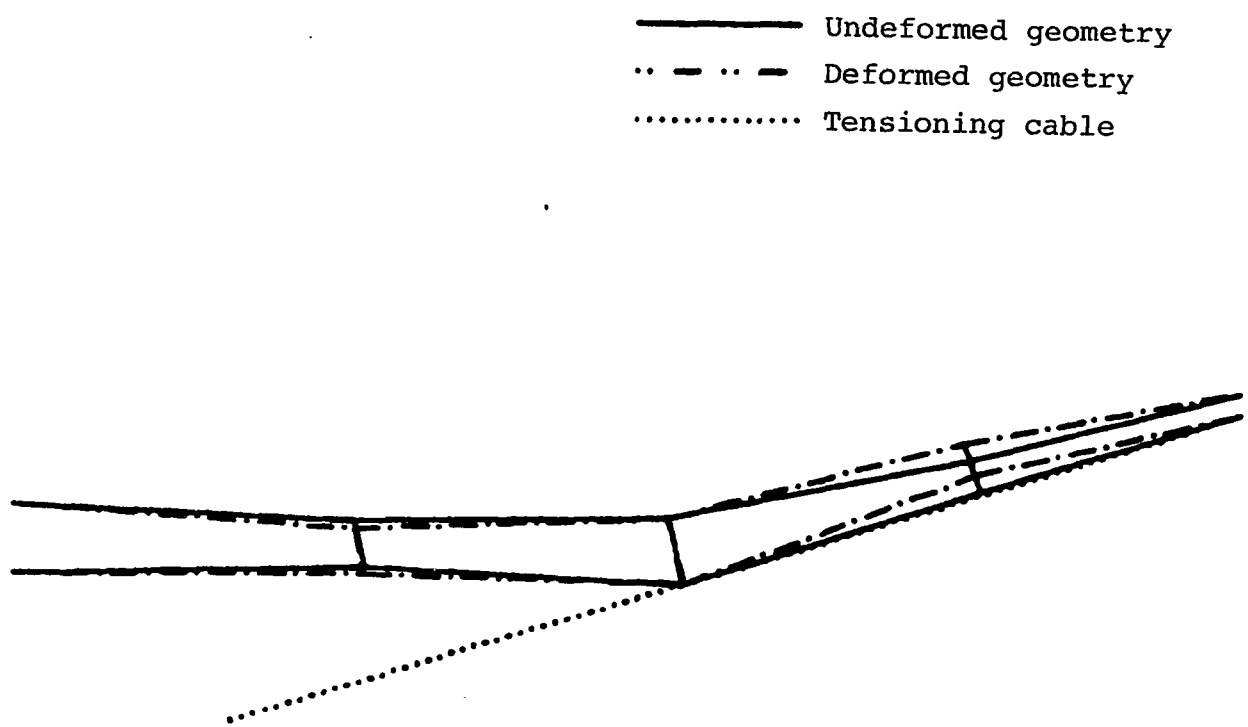

Figure 5.3. Model 1 deformed geometry, $\Delta T = 0°F$

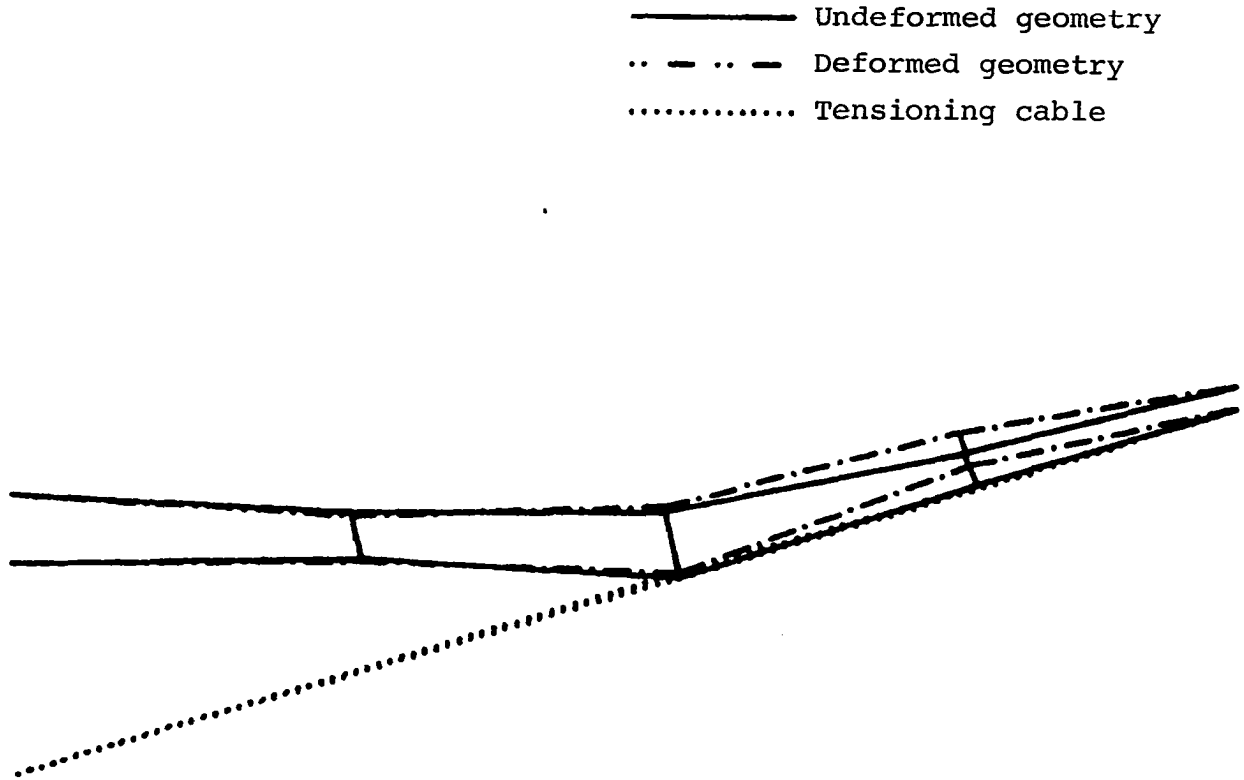

Figure 5.4. Model 1 deformed geometry, $\Delta T = 300°F$

The optimal tensioning loads were determined for the target parabola $y = 0.0002\ X^2$. The results of these runs are contained in Tables 5.5-5.9 which summarize the convergence histories for the temperatures indicated.

The deformed and undeformed structural shapes are shown in Figures 5.10-5.13 for the optimal tensioning loads at the temperatures indicated. The displacements were increased by a factor of 10.0 for these figures. The function $y-\hat{y}$ is shown in Figures 5.14-5.17. The solutions for Model 2 are presented for comparison with the best geometric fit in Figure 5.18.

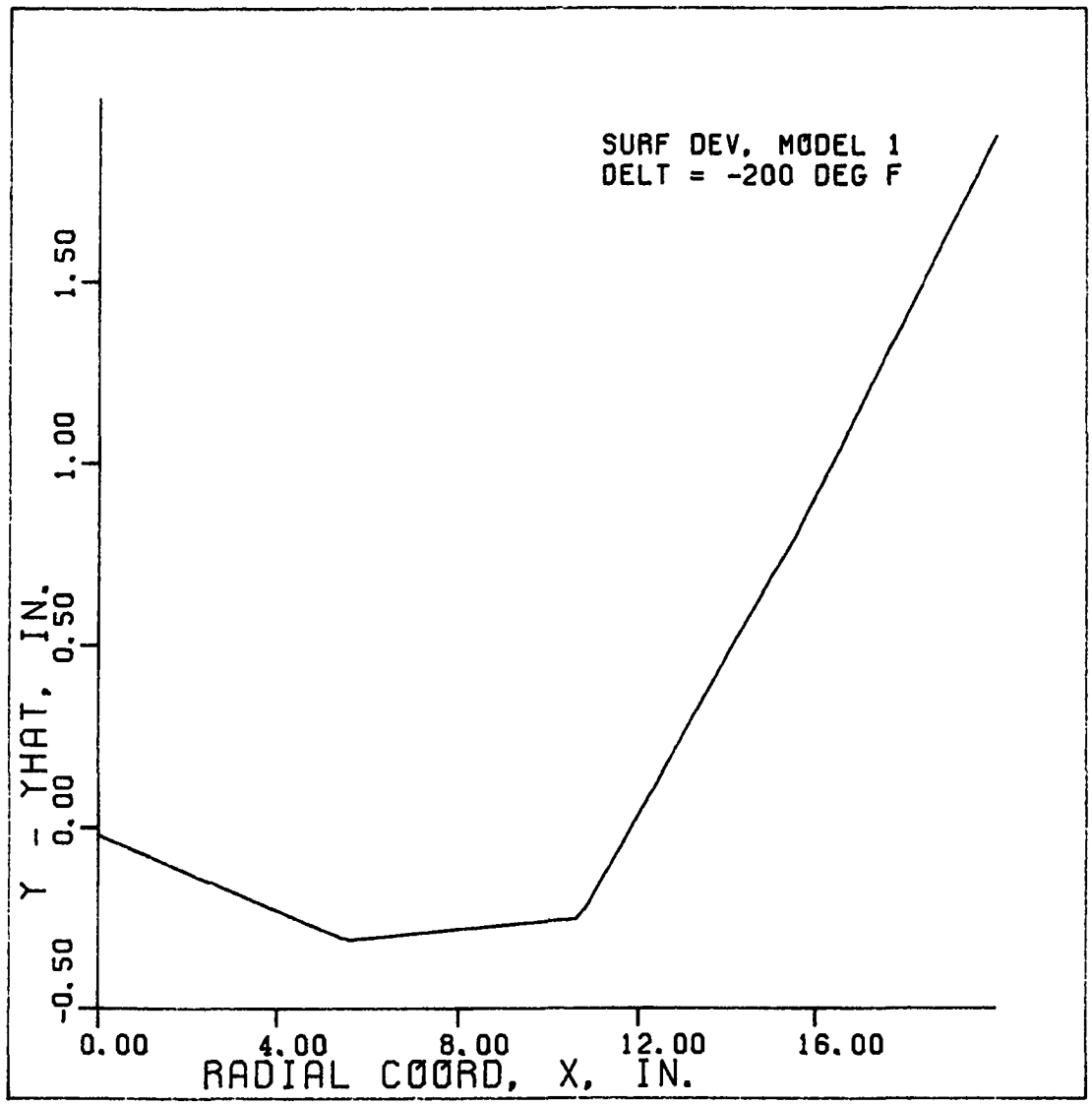

Figure 5.5. Surface deviation, $\Delta T = -200°F$

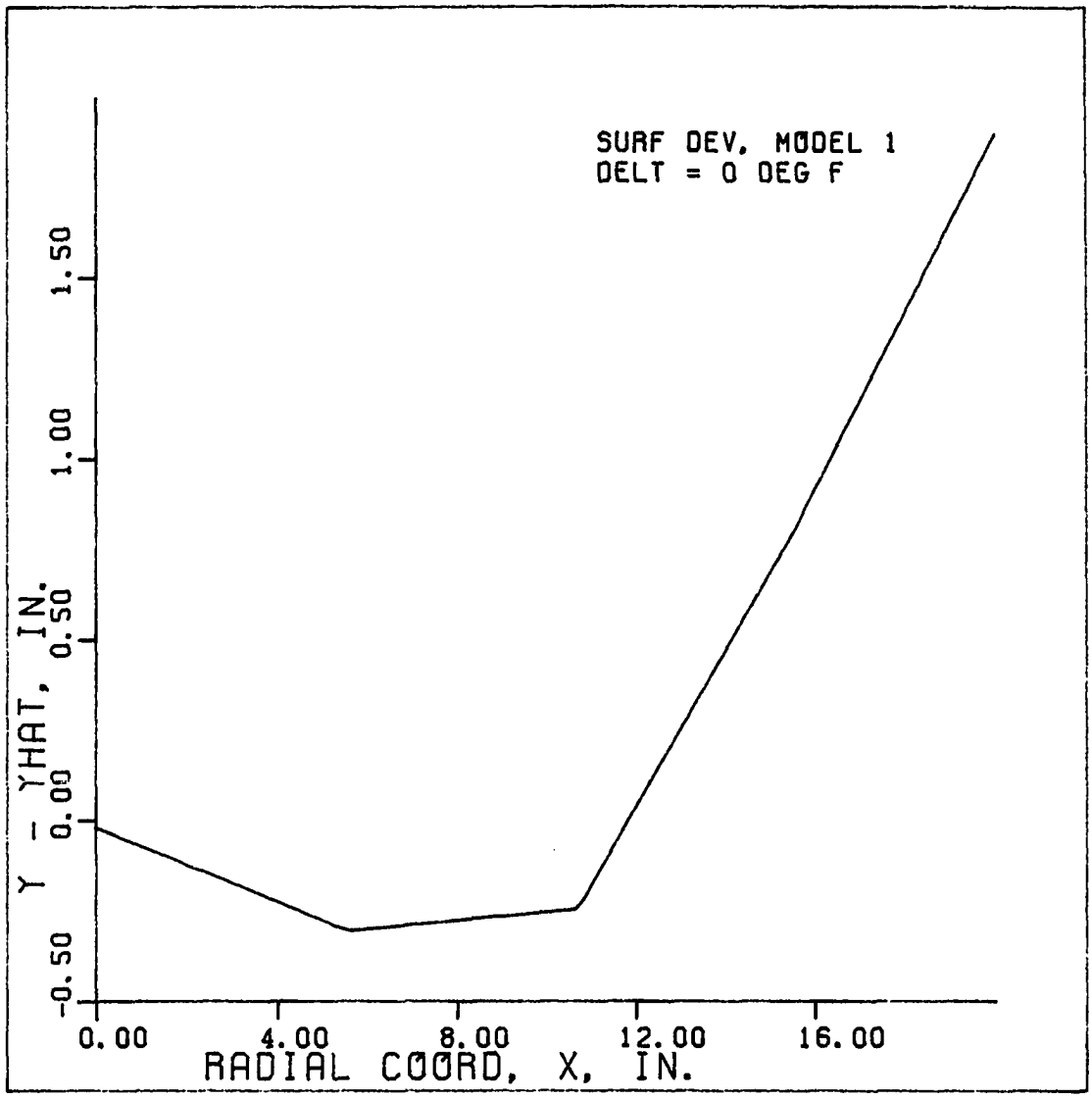

Figure 5.6. Surface deviation, $\Delta T = 0°F$

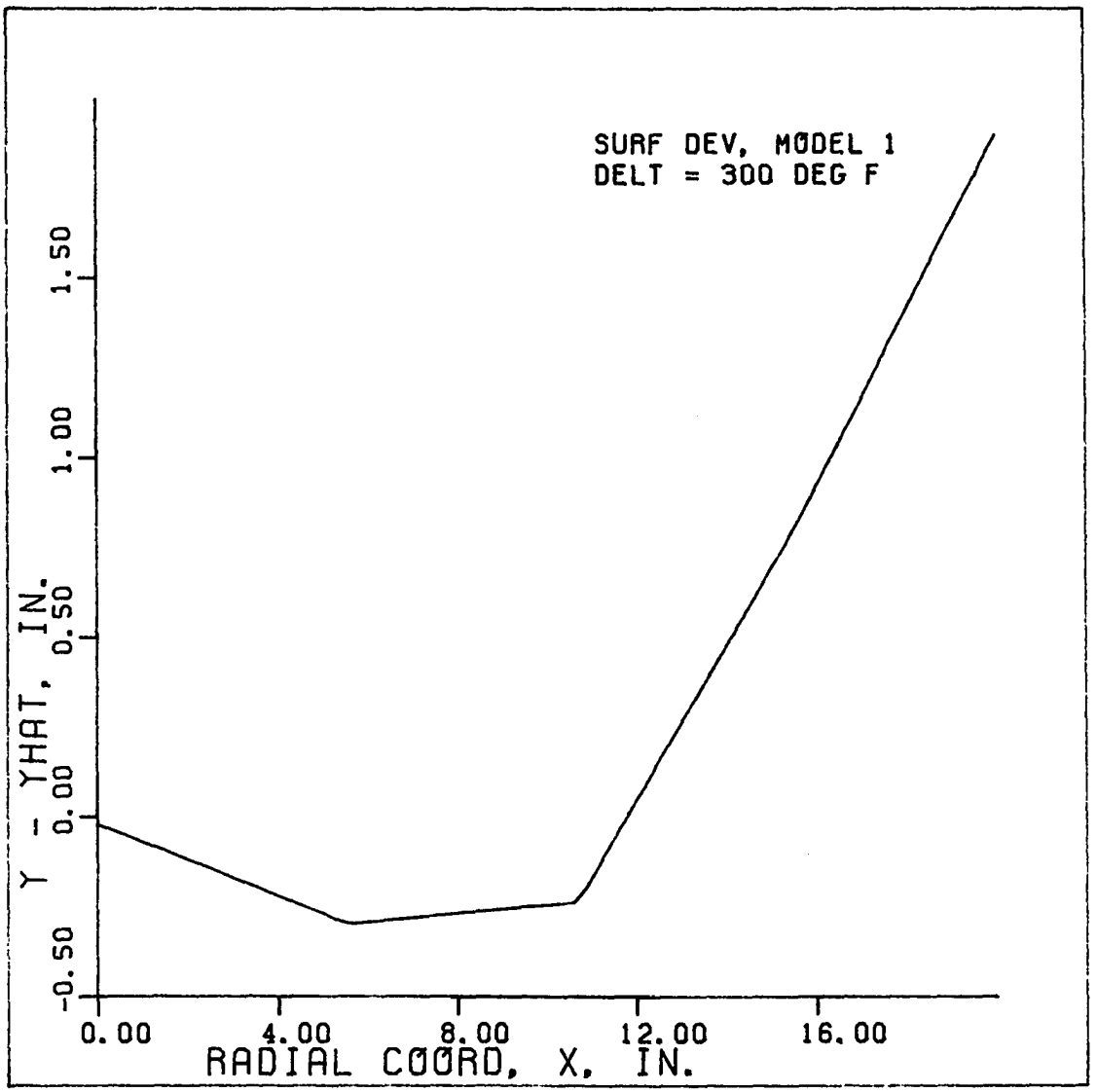

Figure 5.7. Surface deviation, $\Delta T = 300°F$

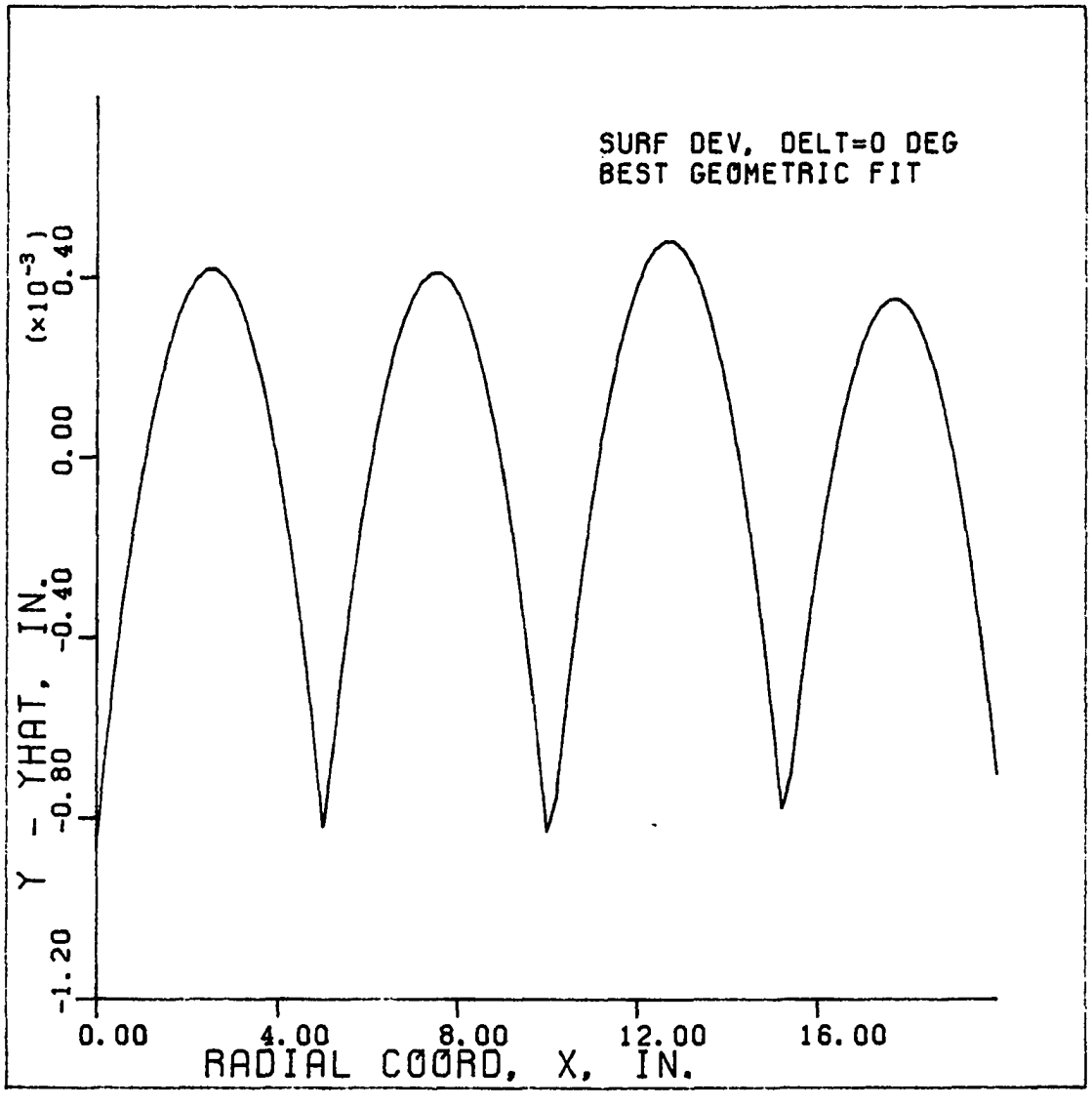

Figure 5.8. Surface deviation - best geometric fit

Table 5.5. Initial nodal coordinates for Model 2[a]

Node	X	Y
1	0.0000	-0.0007
2	0.0000	-1.0000
3	5.0000	0.0193
4	5.0000	-0.6000
5	10.0000	0.0393
6	10.0000	-0.5000
7	15.0000	0.0593
8	15.0000	-0.5500
9	20.0000	0.0793
10	20.0000	-0.6000

[a]Nodes 1, 2, 9, and 10 are completely constrained.

MODEL 2 GEOMETRY

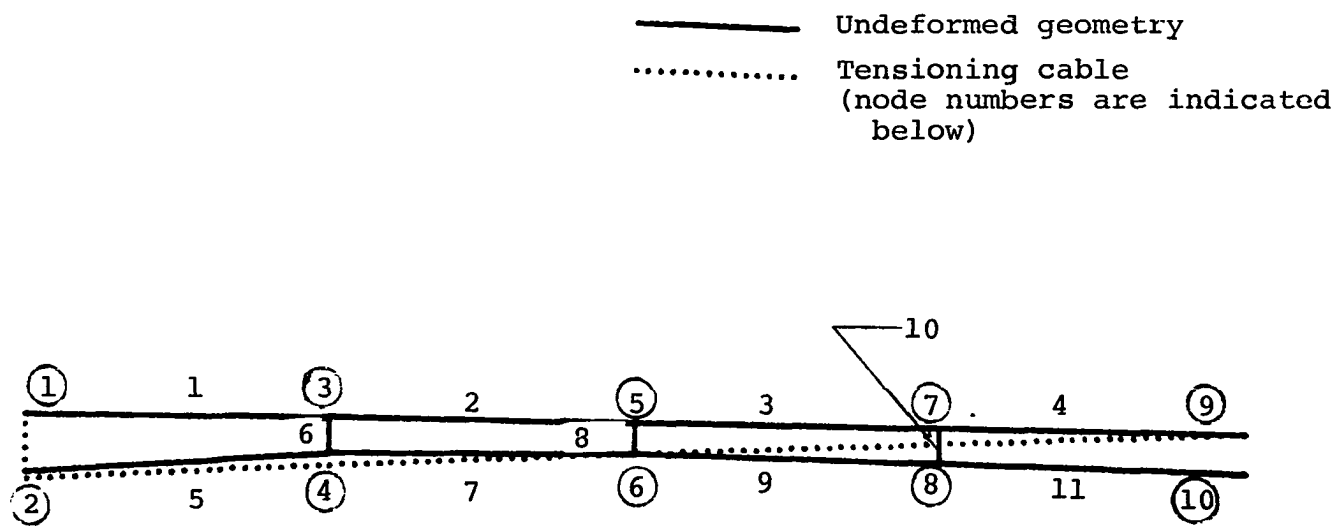

Figure 5.9. Model 2 undeformed geometry

Table 5.6. Optimization history, Model 2, $\Delta T = -300°F$[a]

Iteration	X_1	X_2	$\frac{\partial \Phi}{\partial X_1}$	$\frac{\partial \Phi}{\partial X_2}$	Φ
0	10.897	2.709	$-3.861(10)^{-3}$	$1.451(10)^{-2}$	$4.436(10)^{-2}$
5	26.061	3.045	$-3.917(10)^{-7}$	$-1.574(10)^{-7}$	$8.258(10)^{-3}$
10	26.131	2.907	$-3.640(10)^{-6}$	$6.073(10)^{-6}$	$8.248(10)^{-3}$
15	26.953	3.318	$-5.812(10)^{-6}$	$1.138(10)^{-5}$	$8.247(10)^{-3}$
20	26.955	3.314	$-4.127(10)^{-7}$	$1.590(10)^{-9}$	$8.247(10)^{-3}$
25	26.958	3.315	$3.442(10)^{-7}$	$-1.591(10)^{-6}$	$8.247(10)^{-3}$
30	26.959	3.317	$-7.454(10)^{-7}$	$7.035(10)^{-7}$	$8.247(10)^{-3}$
35	26.981	3.326	$-3.485(10)^{-7}$	$-1.304(10)^{-7}$	$8.247(10)^{-3}$
40	26.984	3.327	$2.671(10)^{-7}$	$-1.430(10)^{-6}$	$8.247(10)^{-3}$
41	26.984	3.328	$-3.748(10)^{-7}$	$-7.475(10)^{-8}$	$8.247(10)^{-3}$

[a]The maximum force imbalance for any degree of freedom is $5.84(10)^{-4}$ lb at the solution. The solution required 149 function evaluations.

Table 5.7. Optimization history, Model 2, $\Delta T = 0°F$[a]

Iteration	X_1	X_2	$\frac{\partial \Phi}{\partial X_1}$	$\frac{\partial \Phi}{\partial X_2}$	Φ
0	10.000	10.000	$-1.588(10)^{-2}$	$1.860(10)^{-1}$	$9.549(10)^{-1}$
5	10.276	7.212	$-2.001(10)^{-2}$	$1.645(10)^{-1}$	$4.715(10)^{-1}$
10	10.764	3.837	$-1.546(10)^{-2}$	$7.746(10)^{-2}$	$5.756(10)^{-2}$
15	10.933	3.039	$-1.146(10)^{-2}$	$4.918(10)^{-2}$	$1.116(10)^{-2}$
18	10.995	2.779	$-7.457(10)^{-3}$	$3.070(10)^{-2}$	$2.642(10)^{-3}$

[a]The maximum force imbalance for any degree of freedom is $3.783(10)^{-2}$ lb at the solution. The solution required 228 function evaluations.

Table 5.8. Optimization history, Model 2, $\Delta T = 100°F$[a]

Iteration	X_1	X_2	$\frac{\partial \Phi}{\partial X_1}$	$\frac{\partial \phi}{\partial X_2}$	Φ
0	10.000	10.000	$-1.806(10)^{-2}$	$2.022(10)^{-1}$	1.088
5	10.172	8.237	$-2.142(10)^{-2}$	$1.922(10)^{-1}$	$7.468(10)^{-1}$
10	10.405	6.341	$-2.302(10)^{-2}$	$1.622(10)^{-1}$	$4.132(10)^{-1}$
15	10.914	3.310	$-1.551(10)^{-2}$	$6.523(10)^{-2}$	$7.140(10)^{-2}$
16	11.005	2.927	$-1.361(10)^{-2}$	$5.198(10)^{-2}$	$5.039(10)^{-2}$

[a]Solution terminated by buckling.

Table 5.9. Optimization history, Model 2, $\Delta T = 200°F$[a]

Iteration	X_1	X_2	$\frac{\partial \Phi}{\partial X_1}$	$\frac{\partial \Phi}{\partial X_2}$	Φ
0	10.000	10.000	$-2.038(10)^{-2}$	$2.193(10)^{-1}$	1.219
5	10.179	8.235	$-2.403(10)^{-2}$	$2.079(10)^{-1}$	$8.492(10)^{-1}$
10	10.330	7.008	$-2.550(10)^{-2}$	$1.892(10)^{-1}$	$6.087(10)^{-1}$
15	10.627	5.032	$-2.362(10)^{-2}$	$1.325(10)^{-1}$	$2.942(10)^{-1}$
18	10.913	3.560	$-1.866(10)^{-2}$	$7.890(10)^{-2}$	$1.434(10)^{-1}$

[a]Solution terminated by buckling.

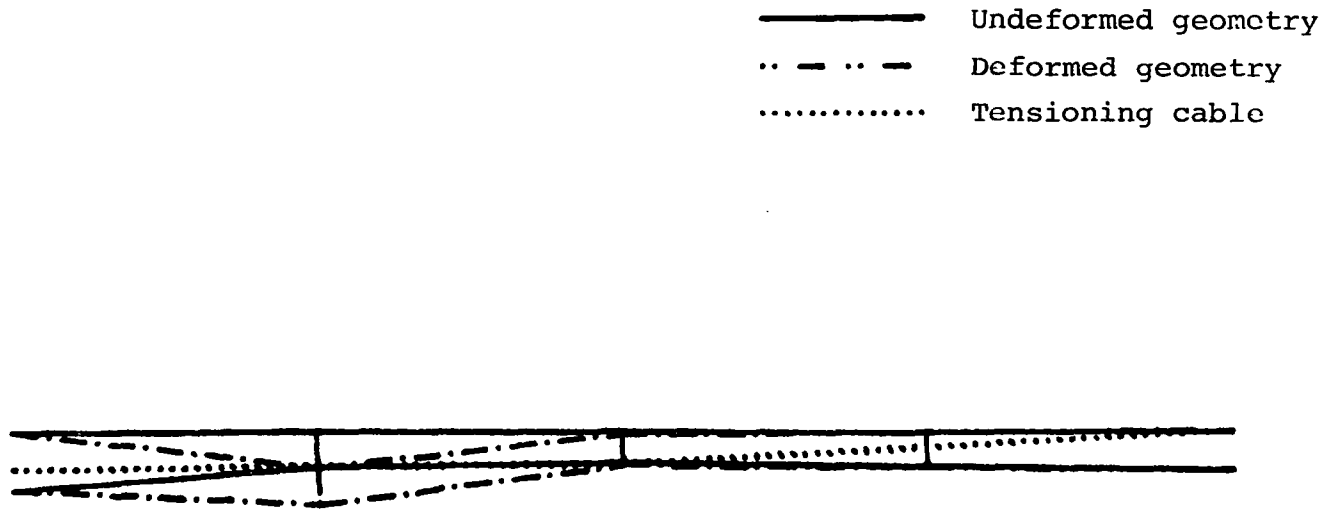

Figure 5.10. Model 2 deformed geometry, $\Delta T = -300°F$

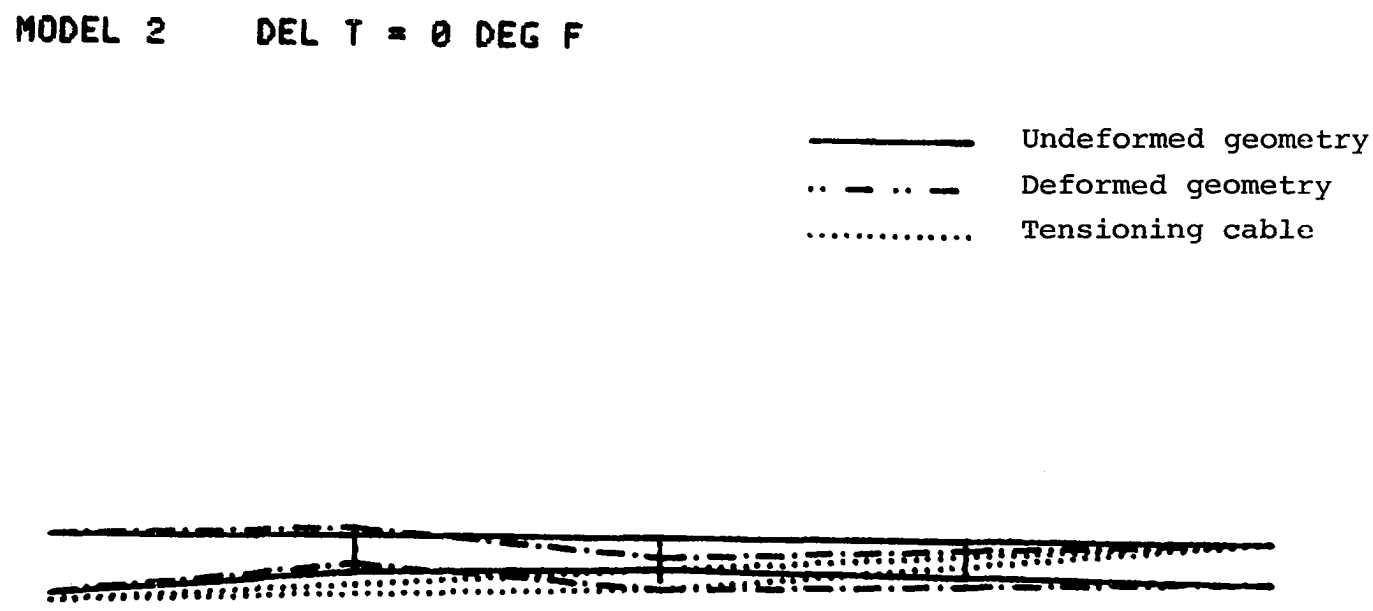

Figure 5.11. Model 2 deformed geometry, $\Delta T = 0°F$

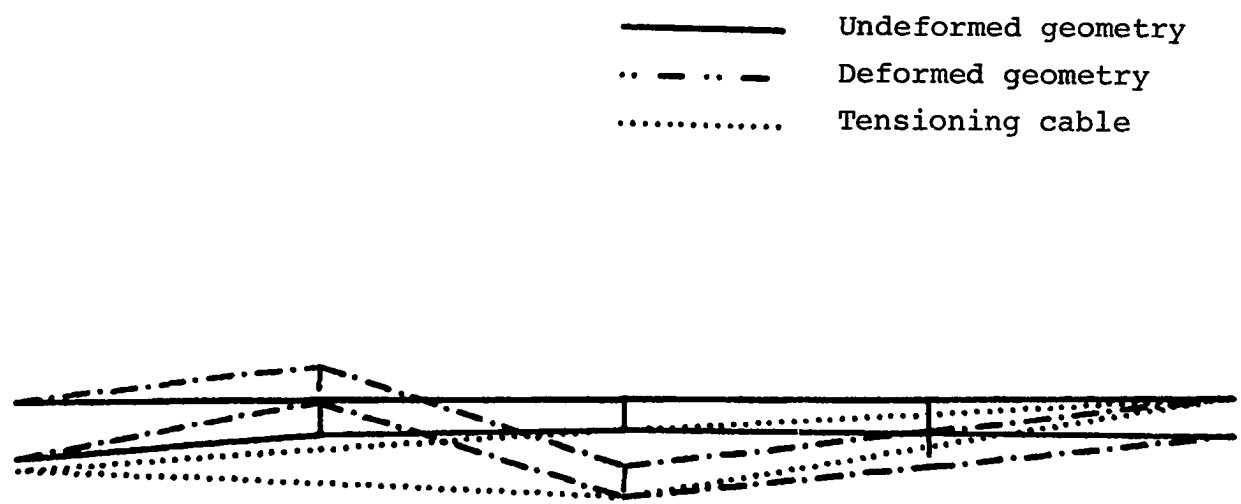

Figure 5.12. Model 2 deformed geometry, $\Delta T = 100°F$

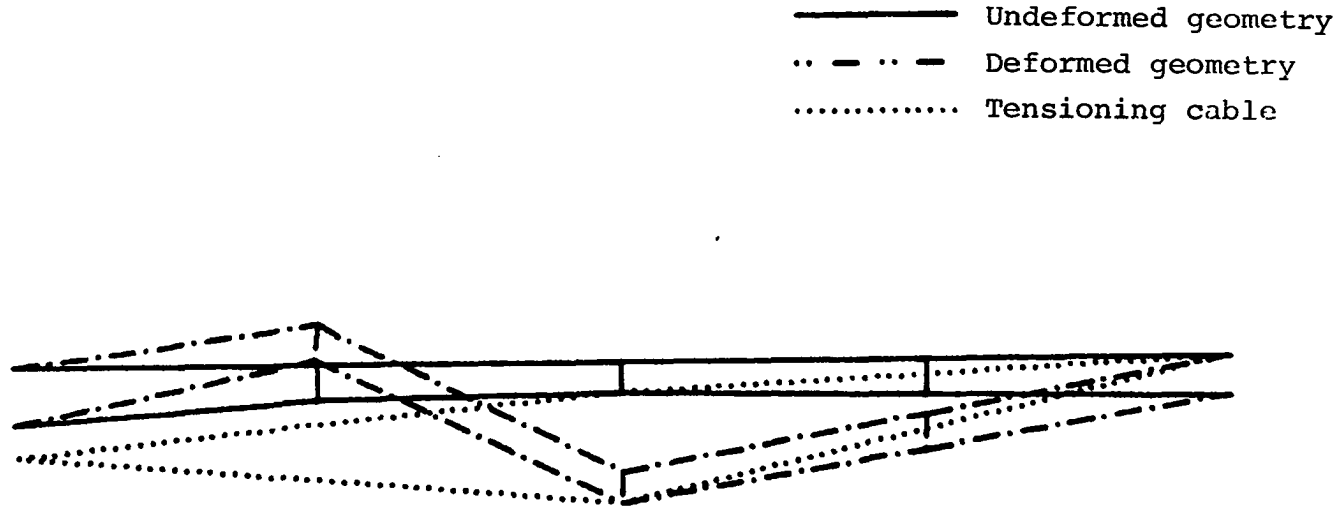

Figure 5.13. Model 2 deformed geometry, $\Delta T = 200°F$

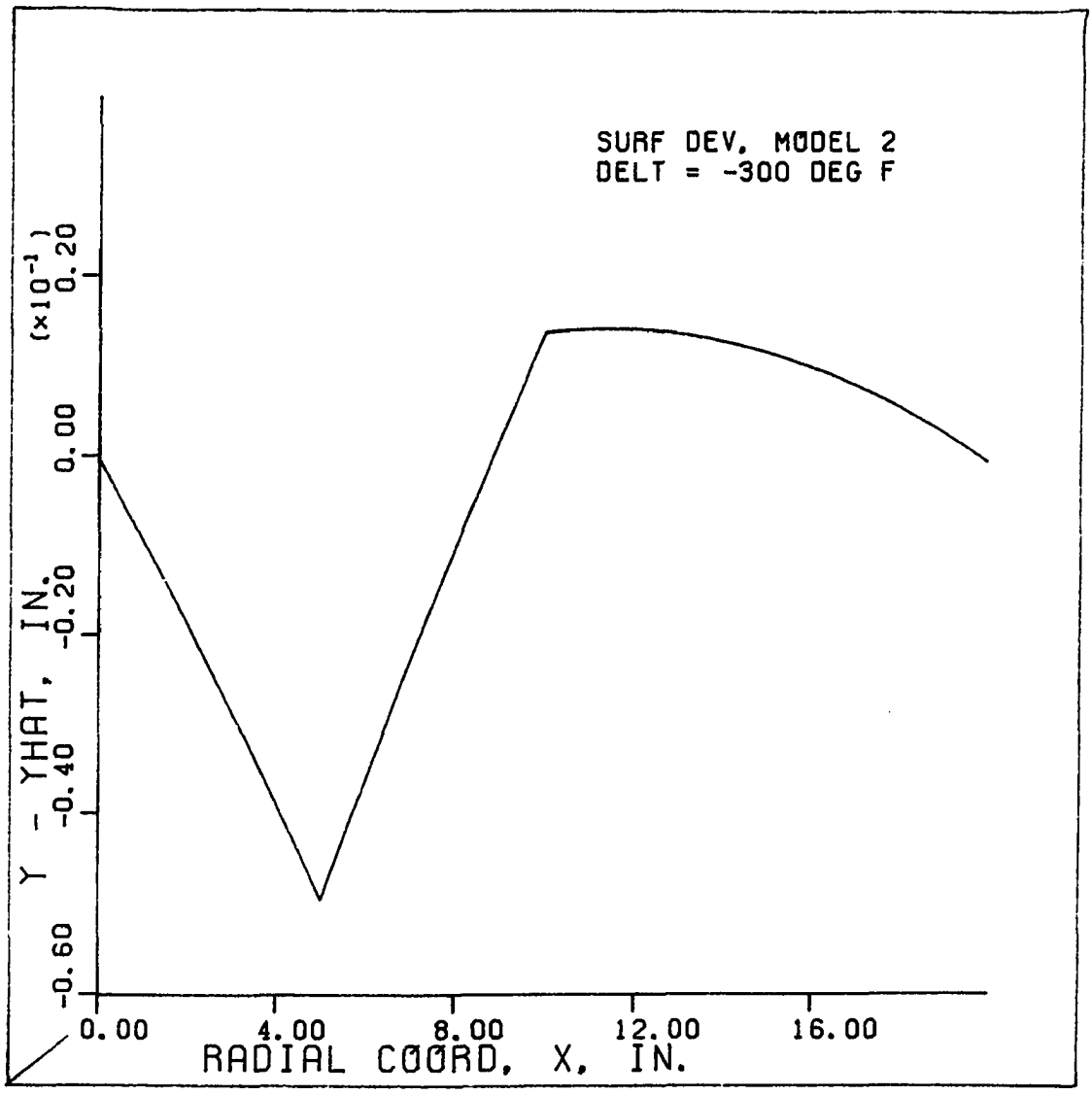

Figure 5.14. Surface deviation, $\Delta T = -300°F$

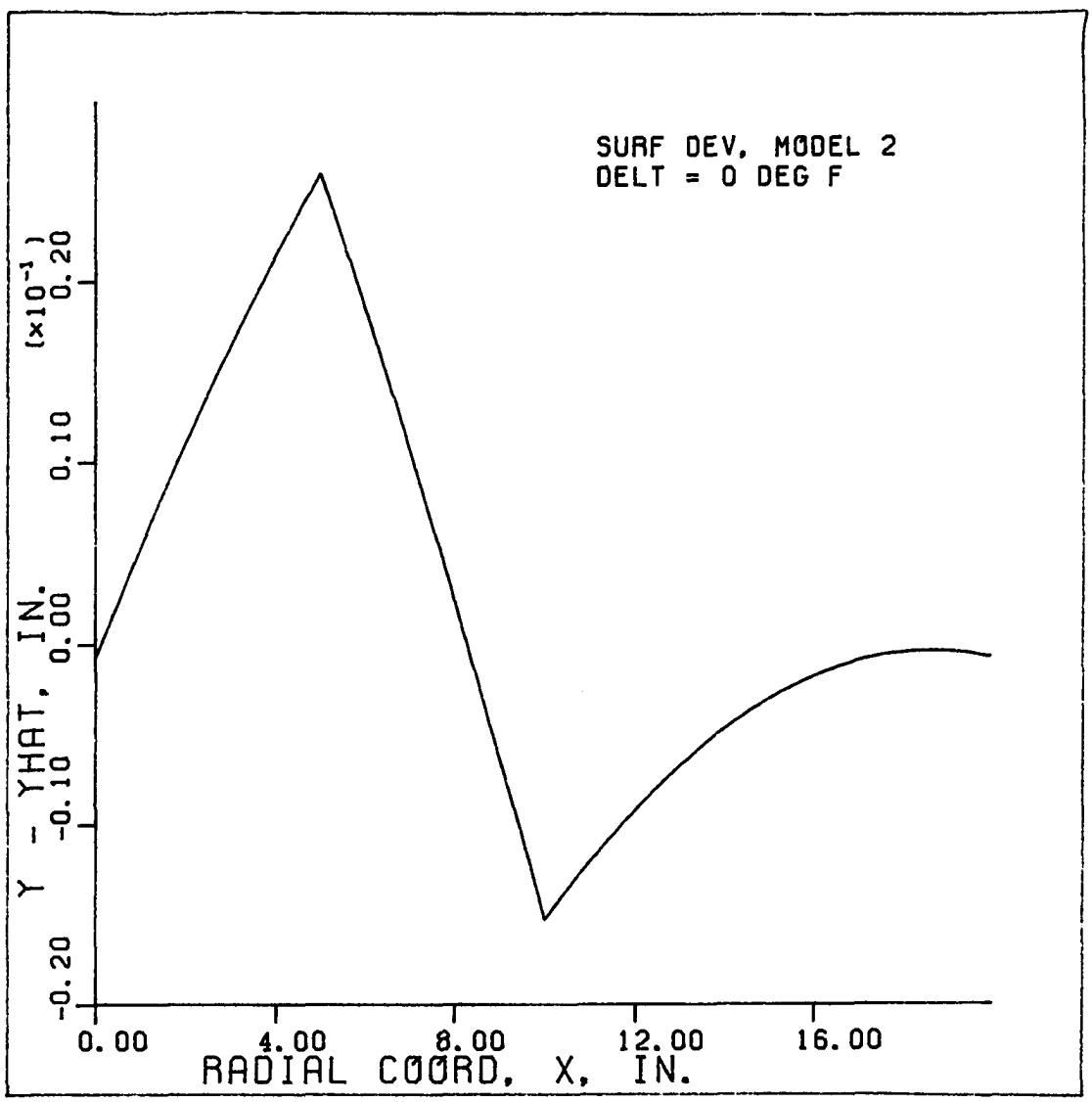

Figure 5.15. Surface deviation, $\Delta T = 0°F$

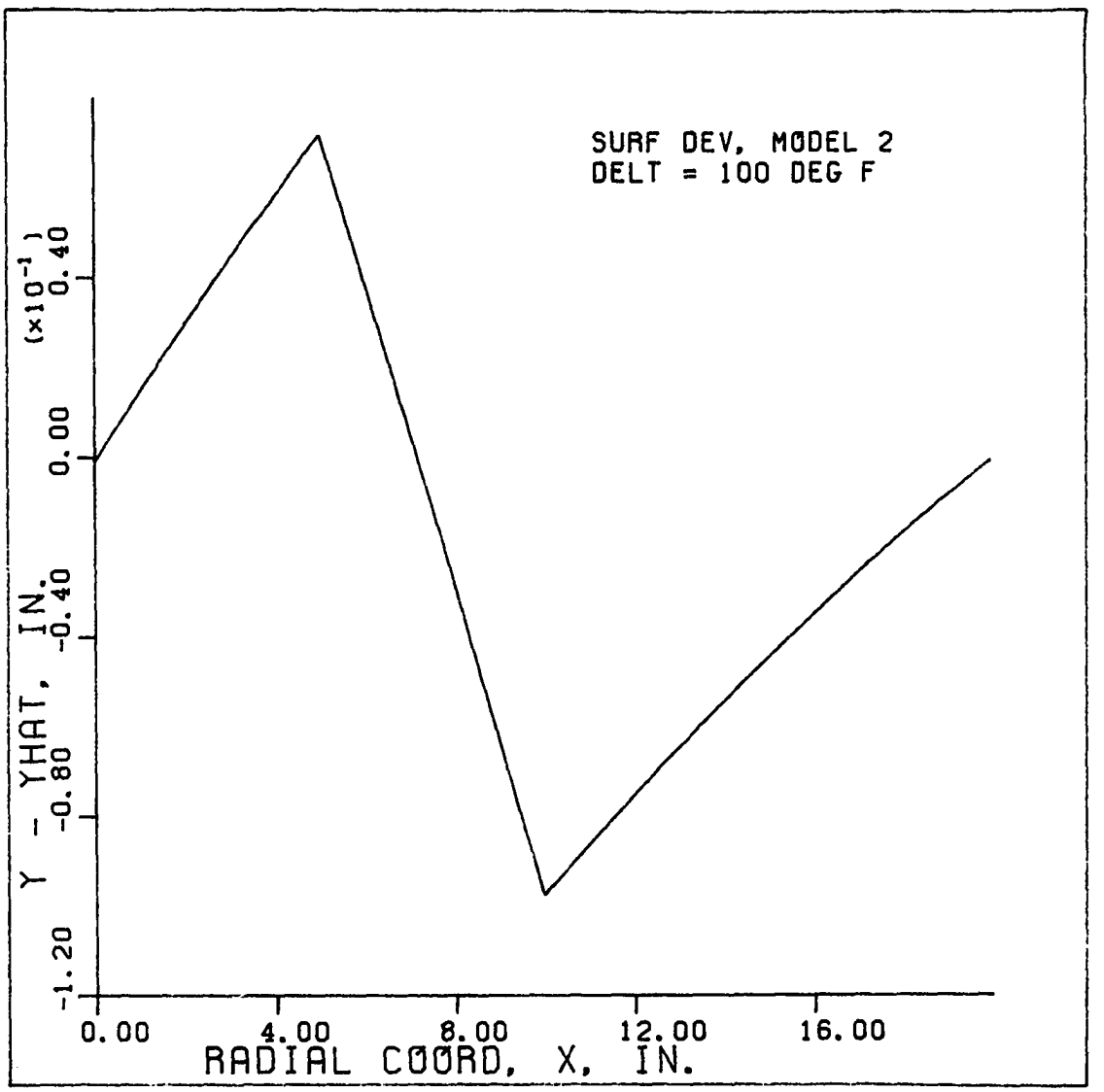

Figure 5.16. Surface deviation, $\Delta T = 100°F$

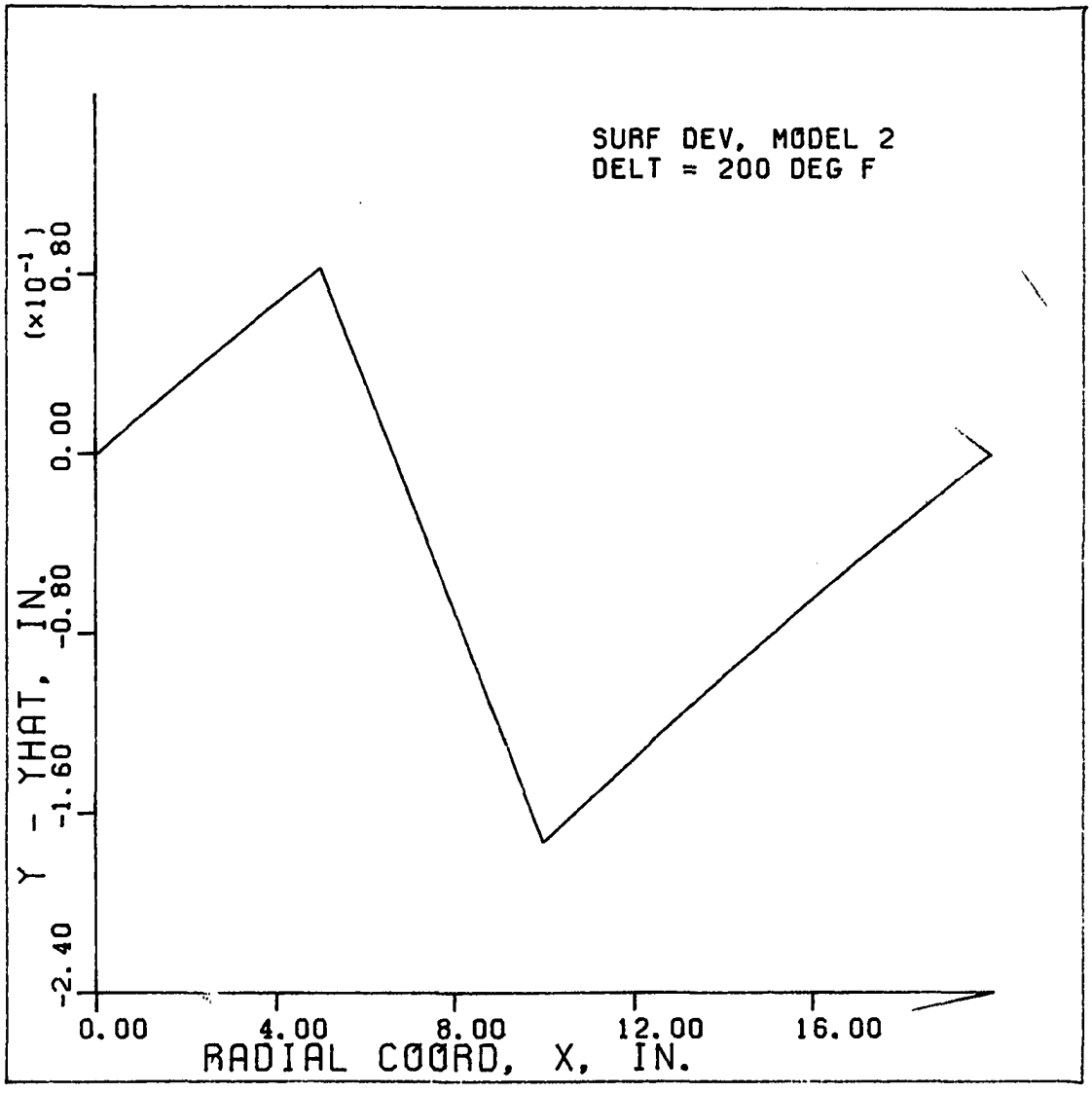

Figure 5.17. Surface deviation, $\Delta T = 200°F$

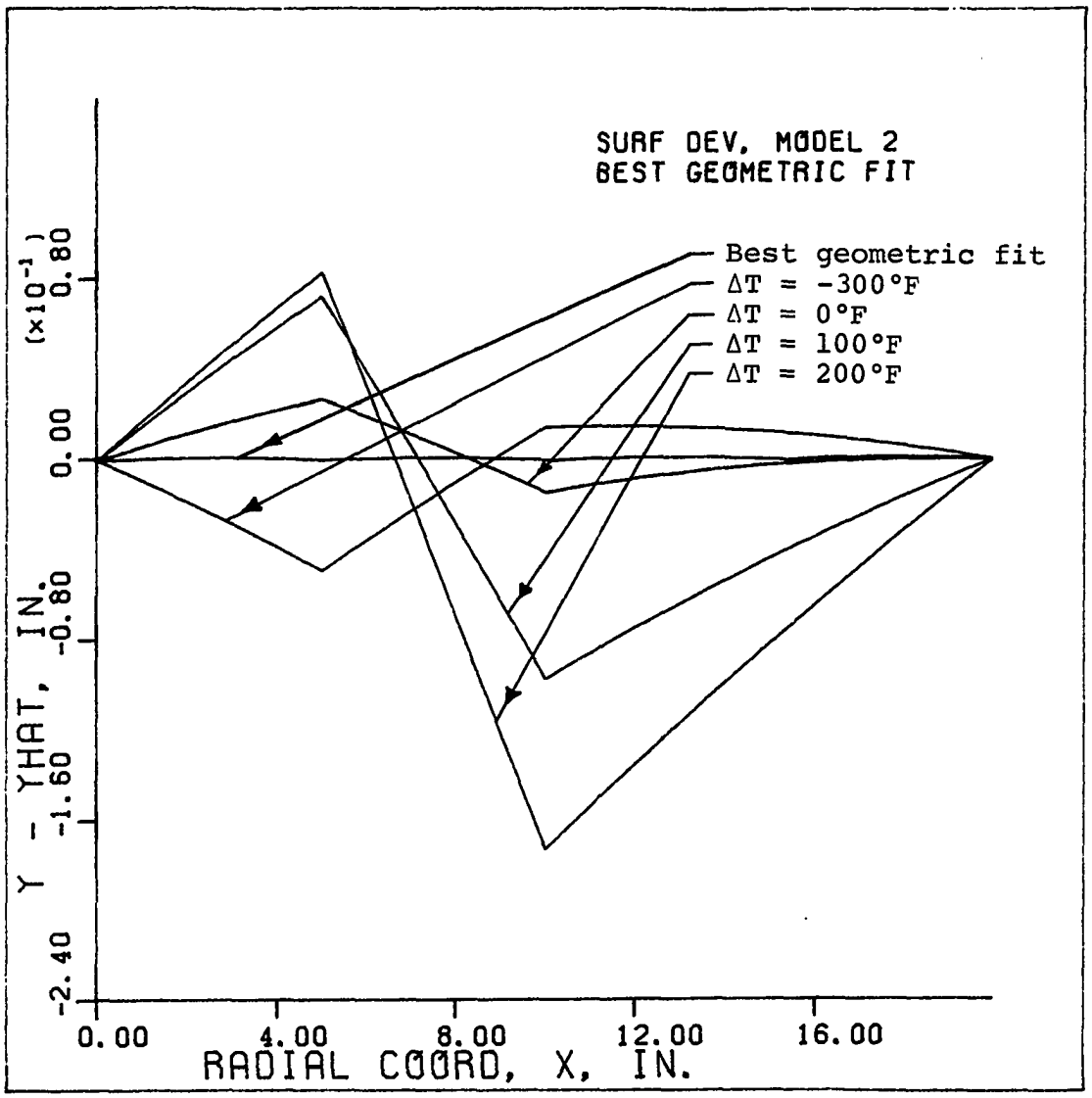

Figure 5.18. Model 2 surface deviation summary

6. DISCUSSION OF RESULTS, CONCLUSIONS, AND RECOMMENDATIONS

The first model studied clearly converges to an optimum solution with the associated near zero gradient vector. These results are disappointing as the objective function was not significantly reduced. Model 2 was generated using different initial geometry in the hope for a more satisfying solution. Indeed, the objective function was significantly reduced for this model by as much as three orders of magnitude ($\Delta T = 0°F$).

The second model demonstrates the need to include buckling constraints in the problem formulation. The solution presented for ΔT's equal to +100 degrees F and +200 degrees F exhibit rather large gradients for an optimal solution. The optimization process did, in fact, buckle the structure in the iteration following the solution presented. These solutions may be considered as an optimum solution from an engineering standpoint since the objective functions have been substantially reduced. They certainly are not optimum solutions from a mathematical standpoint.

Comparing the solutions for the two models leads to the conclusion that the solution is highly dependent upon initial geometry since it is the only difference between Model 1 and Model 2. The optimum solutions for these models

differ by as much as four orders of magnitude. The small reduction in the objective function during the study of Model 1 supports the conclusion that additional degrees of freedom (applied forces) are required to reduce the objective function for this initial geometry.

The results of this study demonstrate that the method will predict optimal tensioning loads while simultaneously satisfying a large number of nonlinear equality constraints. This is a significant accomplishment, as the constraint satisfaction does not require the introduction of either penalty functions or Lagrange multipliers.

The constraint satisfaction requires the solution of a large number of nonlinear finite element equations as a part of the optimization process. As the structural models become large, the number of finite element equations may be prohibitively costly to solve in the optimization algorithm. Two possible remedies exist for this problem, the first is a reduction in the number of equations required to model the problem as reported by Noor (8). The second remedy would be the development of a nonlinear isoparametric antenna rib superelement.

A superelement would allow a large portion of an antenna rib to be modelled by a single element. While such an element would generate more equations per element than the four degree-of-freedom truss element used in the current

study, the total number of equations could be substantially reduced. Far fewer superelements than truss elements would be required to model the structure. Superelements would require significantly more computation time per element than the truss element but this increase is offset since fewer elements would be required.

The current optimization algorithm exhibits many more steepest descent steps than conjugate gradient steps. Examination of the convergence histories in Tables 5.2 through 5.9 further shows that the gradient does not decrease uniformally. This is a result of using the tangent stiffness matrix in gradient computations. Although this algorithm worked well for the two degree of freedom test problems, one would expect the convergence characteristics of this algorithm to deteriorate rapidly as the number of degrees of freedom increases. This is a result of the well-known fact that steepest descent algorithms do not converge nearly as rapidly as do conjugate gradient algorithms.

The large number of steepest descent steps is a consequence of the force imbalance growing unacceptably large. This results from holding the tangent stiffness matrix constant during the optimization routines. Better stiffness data is required, but assembling and reducing the stiffness matrix for every function evaluation during one-dimensional searches is clearly prohibitive. A logical solution to this problem

is the use of a BFGS update (8) for the inverse stiffness matrix.

The BFGS update method allows one to approximately evaluate an "updated" inverse stiffness matrix based upon the old inverse stiffness matrix, force imbalance, and displacement search direction. During the present method, the cable structure is easily buckled, leading to a nonpositive definite stiffness matrix. Small errors in the updated coordinates lead to this problem. The BFGS method must be applied carefully so as to avoid these problems. If one can predict an inverse stiffness matrix by using this method, it will result in a larger number of conjugate gradient steps and far fewer total steps.

The present study demonstrates that the method is a potentially useful tool in antenna design. The two-dimensional capability of the current code is a major deficiency. Since the proposed antennas are very large with multi-band capability, mathematical models of these antennas must possess three dimensional capability for both structural modeling and antenna surface modeling.

The structural model should be capable of modeling the reflective mesh, including the geometrically nonlinear effects and it should model the flexible hoop. The antenna error function can be reevaluated to reflect current design criteria. Any error function which relates antenna error

to a surface shape could be used in this optimization algorithm.

The model should include a realistic number of tensioning loads. It may also be desirable to include a feed position degree of freedom. Such a degree of freedom would allow the optimization algorithm to adjust the target surface as well as the tensioning loads.

7. REFERENCES

1. Thompson, W. and Schultz, J. "Deployable Antenna Demonstration Study", NASA Conference Publication 2035, Vol. I. NASA Langley Res. Center, Hampton, Virginia, Jan. 17-19, 1978, 403-479.

2. Sadin, S. R. "Technology Needs and Opportunities for Future NASA Missions." NASA Conference Publication 2035, Vol. I. NASA Langley Res. Center, Hampton, Virginia, Jan. 17-19, 1978, 19-69.

3. Levy, R., and Melosh, R. "Computer Design of Antenna Reflection." AIAA Paper No. 73-351, AIAA/ASME/SAE 14th Structure, Structural Dynamics, and Materials Conference, Williamsburg, Virginia, March 20-22, 1973.

4. Eldred, D., and Schaechter, D. "Experimental Demonstration of Static Shape Control." Journal of Guidance, Control, and Dynamics, 6, No. 3 (May-June, 1983), 188-192.

5. Bathe, K. J. Finite Element Procedures in Engineering Analysis. Englewood Cliffs, New Jersey: Prentice Hall, 1982.

6. Bathe, K. J., Ozdemir, H. and Wilson, E. L. "Static and Dynamic Geometric and Material Nonlinear Analysis." Report No. UCSESM 74-4, Department of Civil Engineering, University of California, Berkeley, 1974.

7. Bathe, K. J., and Cimento, A. P. "Some Practical Procedures for the Solution of Nonlinear Finite Element Equations." J. Computer Methods in Applied Mechanics and Engineering, 22 (1980), 59-85.

8. Noor, A. K. "Recent Advances in Reduction Methods for Nonlinear Problems." Computers and Structures, 13, (1981), 31-44.

8. ACKNOWLEDGMENTS

The author thanks both NASS-Langley and the Engineering Research Institute of Iowa State University for their support of this work.

Special thanks are extended to Dr. T. J. McDaniel for overseeing this study, and for continued guidance and support throughout the course of this research.

Special thanks are also extended to the author's wife Libby, and parents James and Clara Jean whose support has been an invaluable asset during this research effort.

9. APPENDIX: GEOMETRIC OPTIMIZATION

The error function defined in Equation 2.2 can be minimized with respect to the nodal coordinates x_i, y_i, x_{i+1}, y_{i+1}.

$$\Phi = \sum_{t=1}^{N} \int_{x}^{x_{i+1}} (\hat{y}-y)^2 dx \qquad (2.2)$$

or

$$\Phi = \sum_{i=1}^{N} [\tfrac{1}{5}A^2(x_{i+1}^5 - x_i^5) - \tfrac{1}{2}AB(x_{i+1}^4 - x_i^4)$$

$$+ \tfrac{1}{3}(\beta^2 - 2A\gamma)(x_{i+1}^3 - x_i^3) + \beta\gamma(x_{i+1}^2 - x_i^2)$$

$$+ \gamma^2(x_{i+1} - x_i)] \qquad (2.6)$$

The objective function defined above can be minimized using a standard gradient method since we have defined an unconstrained minimization problem. The required gradient information is contained in Equations 2.12 through 2.15 and is not included here for the sake of brevity. This problem definition is similar to a least squares fit. In a least squares analysis one would determine the parabola which "best" fits the data. In this analysis, we are determining the "best" sequence of straight lines to fit the data. The number of line segments is fixed during this analysis.